Cellulose Nanocrystal Aqueous Inks Evaluated for Printed Electronics and Application to Thin-film Transistors

by

Galina Voloshin

A thesis

presented to the University of Waterloo

in fulfillment of the

thesis requirement for the degree of

Master of Applied Science

in

Electrical and Computer Engineering

Waterloo, Ontario, Canada, 2016

Author's Declaration

I hereby declare that I am the sole author of this thesis. This is a true copy of the thesis, including any required final revisions, as accepted by my examiners.

I understand and accept that my thesis may be made electronically available to the public.

Abstract

With increasing demand for smart features on consumer items, it is imperative that a new class of environmentally sustainable processing methods and materials are developed in order to enable smart functionality on mass produced goods. The challenge faced is to find a suitable material system and process that is bio-sourced, degradable, and compatible with novel substrates for electronics, such as flexible paper and plastic, which are often sensitive to processing conditions. We have demonstrated significant first steps towards this goal through development of conductive, aqueous-based inks of cellulose nanocrystal (CNC) for low-waste additive deposition via inkjet printing. Aqueous CNC dispersions were tuned for printability through addition of ethanol and ethylene glycol before successful patterning unto amorphous silicon (a-Si:H) thin-film transistors (TFTs) as proof-of-concept source and drain contacts. Bio-mass-sourced CNC nanoparticles functionalized with conductive polypyrrole polymer (CNC-PVP-PPY) through oxidative polymerization in water were found to withstand temperatures of 150°C and displayed conductivity as high as 77.8 $S\text{-}m^{-1}$, making this ink a viable candidate to replace conventional polymeric conductors such as PEDOT, which are expensive to produce and require organic solvents and strict processing conditions. Two key observations were made: TFTs fabricated with CNC-PVP-PPY successfully showed switching behaviour with typical mobilities on the order of 0.2 $cm^2V^{-1}s^{-1}$, on-off ratio of 10^6, threshold voltage of 7.6V, and subthreshold swing of 264 mV/dec, however, the larger contact resistance for CNC-PVP-PPY had an impact on the extracted parameters when compared to sputtered metal and printed annealed-silver nanoparticle contact devices. In this work we report the first instance of conductive CNC nanoparticles successfully print-processed from aqueous inks and integrated into a-Si:H TFTs as proof of concept for the use of CNC inks in electronic devices.

Acknowledgements

To my supervisor, Professor William Wong, I extend my gratitude for his support, advice, resources, patience and for enabling the invaluable connections and experiences that have made up my time with the Advanced Flexible Electronics Technology (AFET) group. Great thanks are due to Xinyun (Debbie) Wu and Professor Michael Tam, who developed and provided the materials that are the centerpiece of this work, without them this research would not have been possible.

I give heartfelt thanks for the support and company of everyone in our research group and the Giga-to-Nanoelectronics Lab. Special thanks to Dr. Czang-Ho Lee, who helped with this work through his expertise, time and knowledge, Melissa Jane Chow, who shared with me not only an office but all the frustrating and interesting times setting up our materials printers, and Leon Mintz, who has greatly encouraged me with his enthusiasm and proven that mechanical engineers can indeed transmute into electrical engineers. Thanks also to Richard Barber at the Giga-to-Nanoelectronics Lab, Nicholas Vardy, Rhiannon Lohr, Minoli Pathirane and everyone else I've had the pleasure of working with at AFET.

Finally, I give thanks to my family and my partner, who have supported and motived me through the ups and down of the last two years, for their unfailing belief in my ability to prevail over any challenge.

I dedicate this thesis to my grandfather, Dr. Vladislav Dudko, who is a man of many talents, my academic role model and greatest inspiration for pursuing higher education.

Table of Contents

List of Figures

List of Tables

1   Introduction

This thesis explores a new class of nanomaterials known as cellulose nanocrystals (CNC), which have been functionalized with conductive materials and formulated into printable water-based inks. These inks were studied and used to demonstrate printed source and drain contacts to hydrogenated amorphous silicon (a-Si:H) thin film transistors (TFTs) fabricated using a traditional plasma-enhanced chemical vapour deposition (PECVD) process. The devices were then compared to a-Si:H TFTs with sputtered chromium metal contacts and printed nanoparticle silver (Ag-NP) ink contacts. Ag-NP inks are currently one of the most widely available and extensively-studied conductive inks used in printed electronics, however their high cost and need for post-processing with an annealing treatment are significant drawbacks for use on flexible or paper- based substrates. In comparison, the complementary relationship between inkjet printing and CNC materials allows for low cost, low waste, additive manufacturing fabrication of conductive traces on a variety of substrates including plastics and paper as no annealing step is required. The work described in this thesis is the first instance of conductive CNC materials being developed into aqueous inks, characterized, and inkjet printed for electronics applications.

The base hypothesis of the work is that inkjet printing can provide a highly synergistic relationship with biodegradable and aqueous-based CNC inks if it can be shown that these materials are 1) able to be formulated into printable inks, 2) show conductive behaviour, and 3) behave similarly to incumbent materials, such as silver nanoparticle inks, when integrated into thin-film transistors. In this report, we demonstrate that it is possible to formulate polypyrrole-coated CNC materials into electronic inks which possess desirable printing behaviour and drying properties and fulfill the three criteria above. As the materials are renewable and biodegradable, using no harsh solvents, it is a significant first step forward towards developing a 'green' materials platform for printable electronics that are environmentally sustainable, functional, and degradable.

2 Crystalline nanocellulose

2.1 Structure and properties of cellulose
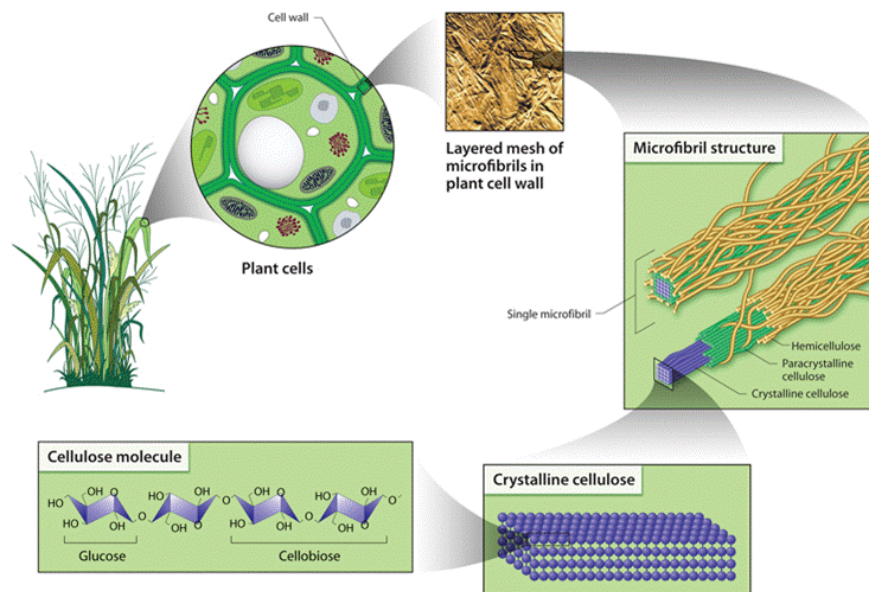
Figure 1 Macro- and micro-structures formed by cellulose polymers. (U.S. DOE Genomics Roadmap: Systems Biology for Energy and Environment, 2005)

Cellulose is a straight-chain carbohydrate polymer composed of repeating units of glucose. Cellulose wields three hydroxyl groups per anhydroglucose unit (AGU), providing the cellulose polymer with a high functionality and affinity for hydrogen bonding, which creates crystalline domains. Cellulose consists of both amorphous and crystalline regions; the combination of these domains creates microfibril structures that weave into layered mats and make up plant cell walls. It is thus an abundant material naturally found in plant biomass due to its role as one of the fundamental building blocks of plant matter. Cellulose is regularly consumed by people in the form of fruits and vegetables, or in the form of dietary fiber as a regulatory agent for our digestive systems. As such it is a biodegradable, renewable and non-toxic material.

Most importantly, it is a low-cost, abundant and 'green' material which can also be used as a platform for flexible lightweight electronics components for energy storage, smart packaging, displays, and more.[1] Recent work with cellulose materials in the field of electronics

demonstrated cellulose used as a simultaneous dielectric and substrate for pentacene OTFTs[2], a battery separator layer in printed flexible batteries[3], and developed into a piezoelectric paper consisting of cellulose pulp specially treated in order to align the fibers and generate a piezoelectric material that acts as both sensor and actuator[4].

2.2 **Crystalline nanocellulose**

By exposing cellulose sources such as cotton to acid through a process known as acid hydrolysis, it is possible to dissolve away the less dense amorphous regions of cellulose fibers and leave only the crystalline regions. Proper treatment with acid will result in a negatively charged surface of hydroxyl groups that acts to stabilize the cellulose suspension and prevent agglomeration. These crystalline nanocellulose (CNC) particles are spindle-like, medium-aspect-ratio rods with diameters in the tens of nanometers and lengths in the range of several hundred nanometers as seen in Figure 2. The specific dimensions of CNC depend on various factors such as the source of cellulose and conditions of the acid hydrolysis such as the type of acid, temperature, and time.[5] Cellulose sources comprise a broad range of plant matter spanning across wood pulp, sugar beet pulp, wheat straw, soy hulls, sisal, palm trees, carrots, and more.[6]
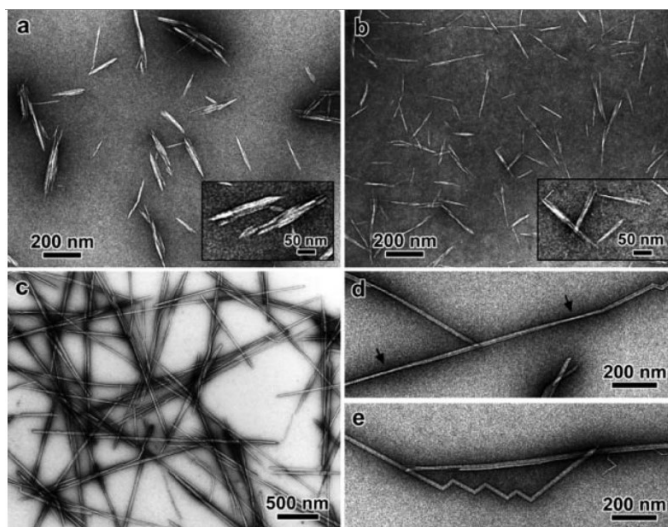
Figure 2 Nanocrystals produced from hydrolyzed a) cotton, b) avicel, c) -e) tunicate cellulose. (Elazzouzi-Hafraoui et al., 2008)

Crystalline nanocellulose materials have intriguing optical, mechanical and chemical properties which have enabled their use as bulk materials, additives, and templates. CNC has been demonstrated in iridescent and transparent films[7],[8], aerogels[9], supercapacitors[10] and composite materials with enhanced mechanical properties.[11] In the space of electronics, nanocellulose paper has been demonstrated in prototype devices as a dual-purpose substrate and dielectric layer for building Gallium Indium Zinc Oxide (GIZO) TFTs.[12] It has also been shown by Wu et al. that functionalizing CNC with conductive polymers such as polypyrrole can be an effective technique to create a new generation of supercapacitor materials on par with single wall carbon nanotubes (SWCNTs).[10] However, despite the promising properties of the wide variety of CNC materials developed, no work has thus far been carried out to deposit and integrate conductive materials templated using CNC into electronic devices.

A primary reason for the increased interest in CNC as a template or filler material comes from the excellent opportunities for functionalization available due to the presence of cellulosic hydroxyl groups. As shown in Figure 3, cellulose nanocrystals can be functionalized in multiple ways such as esterification, TEMPO-oxidation, polymer grafting, silylation, and more.[5] In this work we take advantage of CNC nanoparticles that have been modified using the TEMPO oxidation technique and coated with conductive materials through the process developed by Wu et al.[10] CNC has also been shown to self-assemble under the influence of an AC electric field and magnetic field[13]; the ability to form ordered domains may have interesting implications for CNC coated in charge transporting materials.
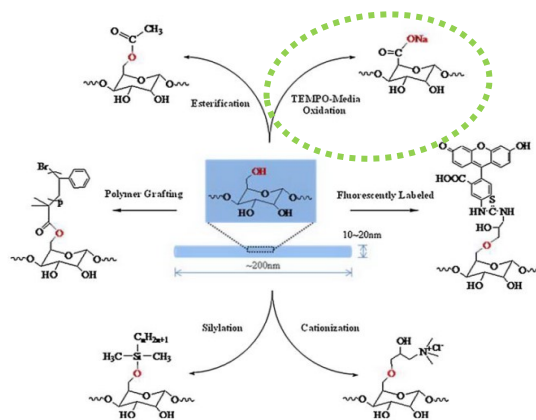
Figure 3 Functionalization mechanisms for modifying the surface chemistry of cellulose nanocrystals (Peng et. al 2011)

As the surface of CNC imparts an excellent stability in aqueous solutions,[5] it can also be used to solubilize grafted materials that have poor solubility in water on their own. This behaviour has been demonstrated by polymerization of pyrrole monomer in water without CNC as a template in contrast to CNC-templated pyrrole; the results reported by Wu et al. and shown in Figure 4 display that under the same polymerization conditions, the CNC-containing solution is homogeneous and well dispersed, while the polypyrrole-only solution has crashed out.
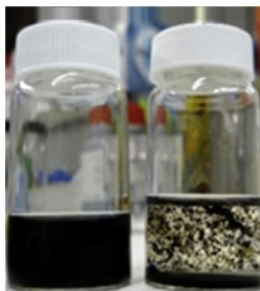
Figure 4 Polypyrrole polymerized with CNC nanoparticles (left vial) and without (right vial) showing significant improvement in solubility.[10]

The potential for application of conductive CNC materials in inkjet printing for development of 'green' aqueous inks has not been previously evaluated and the materials synthesized and used for the work herein are thus being formulated and tested for conductivity, printability and application as a printed thin film transistor contact material for the very first time.

2.3 Synthesis of conductive CNC

In this work we acquired CNC functionalized with poly(3,4-ethylenedioxythiophene) polystyrene sulfonate (PEDOT:PSS), poly(3,4-ethylenedioxythiophene) p-toluenesulfonic acid (PEDOT:PTSA), polypyrrole (PPY), and silver nanoparticles (Ag-NP) that were prepared using previously published methods described by Wu et al.[10] as well as Shi et al.[14] The general

synthesis process for CNC functionalized with PPY (CNC-PPY) is shown in Figure 5 and explained herein.

In all cases CNC is first activated using TEMPO oxidation in order to convert primary hydroxyl groups present on the particle surface into carboxylate groups. Next, pyrrole monomer is added and forms hydrogen bonds between the amine group on the monomer and the carboxyl group on the activated CNC. Finally, an oxidizer such as ammonium persulfate (APS) or ferrous chloride ($FeCl_3$) is added to initiate polymerization of pyrrole groups attached on the CNC nanoneedles and in solution.
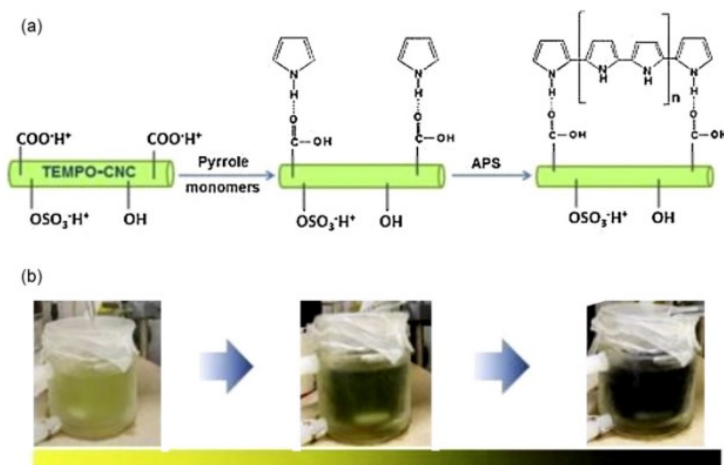
Figure 5 Left: Synthesis process for templating polypyrrole on CNC by means of TEMPO oxidation followed by polymerization in aqueous media.[10]

The synthesis process results in a dark-colored suspension of CNC-PPY nanoneedles which upon freeze-drying and pressing into a pellet showed a good conductivity of 4.5 S/cm as determined by four-point probe.[10] A minor improvement which comprised pre-coating samples of CNC with a layer of polyvinylpyrrolidone (PVP) was done in the case of polypyrrole-coated CNC (CNC-PVP-PPy) in order to improve the coverage of polypyrrole on the CNC surface. The improvement in surface coverage and aspect ratio can be seen in Figure 6 with a more uniform and consistent shape of CNC-PVP-PPY as compared to CNC-PPY. The synthesis process of other conductive polymer-coated cellulose nanocrystals is similar, requiring only the substitution of the desired monomer and a compatible solvent. CNC with silver nanoparticles (CNC-AgNP) was prepared by reducing

silver salt on the surface of polydopamine-functionalized CNC, as outlined previously by Shi et al.[14]

Among the class of conductive polymers, polypyrrole has attracted significant attention due to its ease of preparation, high conductivity and excellent stability. Polypyrrole has one of the lowest oxidation potentials (0.8V) out of the class of heterocyclic monomers, and one that is lower than that of water. This property makes it one of the few conductive polymers that can be synthesized in aqueous solvents.[15] Though the polymer is neutral and non-conducting initially, charge carriers are generated when the material is oxidized, creating polaron or bipolaron states.[16] This behavior is a boon for ambient temperature processing techniques such as inkjet printing as no special environmental control is required, as well as for stability of devices based on polypyrrole as there is no need for encapsulation. For these reasons, polypyrrole applied on CNC was of particular interest due to its promising synthesis route, high conductivity, and stability. All
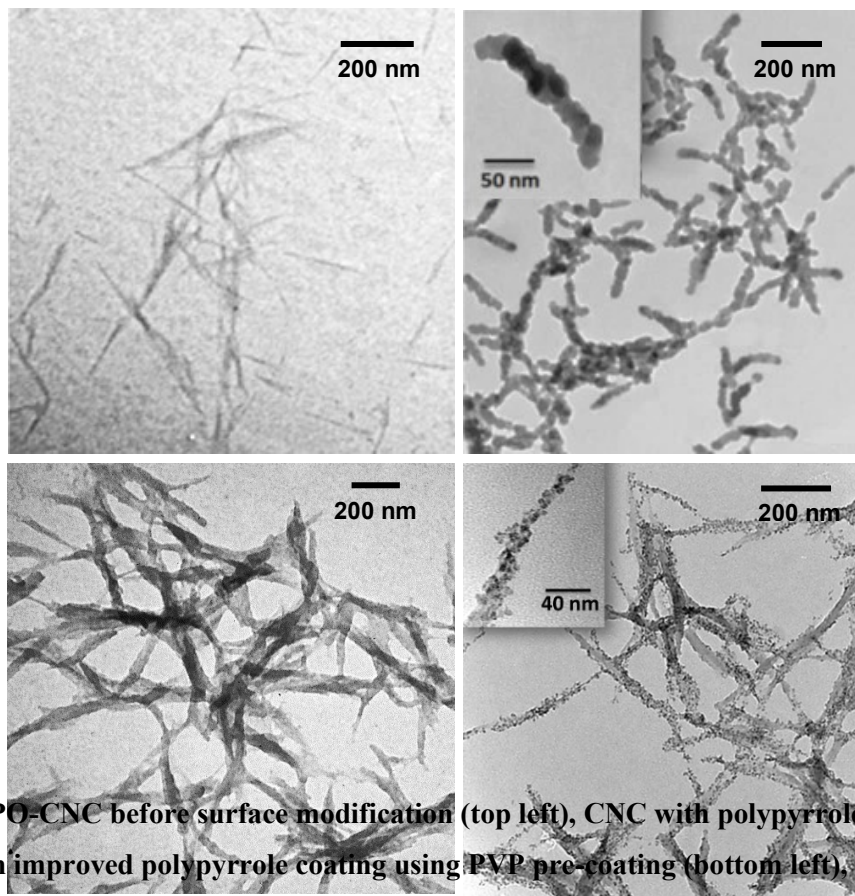
Figure 6 TEMPO-CNC before surface modification (top left), CNC with polypyrrole coating (top right), CNC with improved polypyrrole coating using PVP pre-coating (bottom left), and CNC with silver nanoparticle coating (bottom right) imaged by TEM. (Credit: X. Wu)

materials used in this work were obtained in the form of washed, as-synthesized aqueous suspensions and used as-is.

2.4 **Percolation network theory**

The rationale behind exploring cellulose nanocrystals lies precisely in their ability to act as a nano-sized template for growing other materials. The CNC surface can be used as a textured platform upon which conductive materials are deposited and grown as described previously. This approach greatly reduces the amount of material required to create a conductive network as the material forms a core-shell morphology as shown by the schematic in Figure 7.
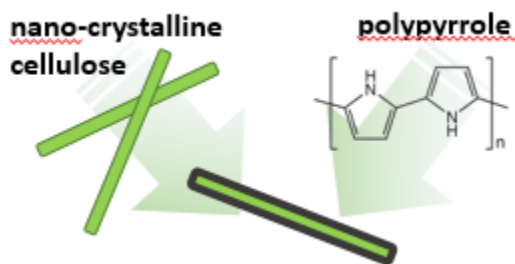
Figure 7 Schematic representation of nano-crystaline cellulose rod coated with polypyrrole.

It is thus possible to create a sparse conductive network at a fraction of the material volume necessary in a bulk film. This concept falls under the umbrella of percolation theory which aims to describe how conductive pathways form when particles of certain dimensions and concentration are randomly arranged in two or more spatial planes (e.g. a 2D mesh or a 3D network). Typical examples of percolation networks are silver nanowires[17][18][19] and carbon nanotubes (CNTs)[20], where overlapping rod-like particles form a pathway for charge transport. For a flat 2D mesh there exists a critical point of surface coverage dubbed the percolation threshold, at which nanoparticles randomly distributed on a substrate transition from an open circuit of unconnected particles to a network providing conductive pathways. The percolation threshold depends on the geometry of the particles, and particularly the ratio of length to width which is known as the aspect ratio. The impact of geometry can be understood by imagining how high aspect ratio wires can bridge a gap with less material and form a connected network at a lower area coverage than a

network of spheres. Large aspect ratio particles are thus desirable when the goal is to form a conductive network with minimal material.

The dimensions of CNC particles functionalized with polypyrrole were characterized and used to determine the percolation threshold for CNC inks. At the percolation threshold, the fractional area covered by particles is defined as $1 - p$, where $p = p_c$ is the critical percolation threshold. A geometry of randomly oriented ellipsoid particles forming a 2D mesh has been simulated by Xia and Thorpe[21] for the 'needle-like' ellipse limit as in the case of nanowires. The critical percolation threshold for a system with this geometry can be approximated as,

$$p_c \approx 1 - \frac{16}{3} b/a, \quad a >> b \tag{1}$$

where a and b are the long and short edges of a particle, respectively, and b/a is the aspect ratio. Cellulose nanocrystals imaged using High Resolution SEM (HRSEM) and shown in Figure 8 had mean lengths and diameters of 369±60 nm and 30±4.4 nm, respectively, as measured by ImageJ processing software. (http://www.imagej.net)
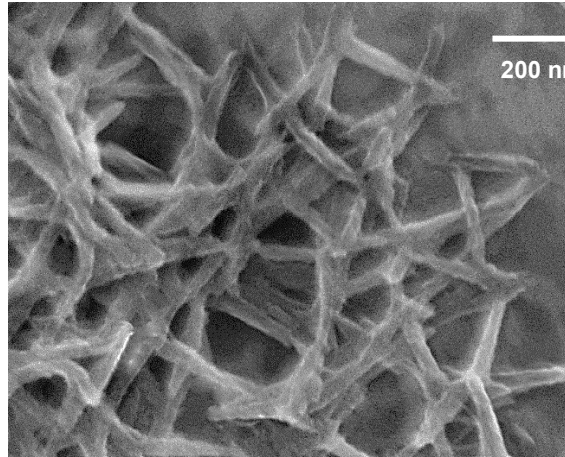
Figure 8 HRSEM image of CNC-PVP-PPY showing the length and diameter of nanoneedles.
(Credit: X. Wu)

For these CNC particles the aspect ratio b/a is ~0.081 and the needle-like approximation for percolation applies. Using Eqn. (1) we can determine that p_c = 56.6% area coverage, thus the percolation threshold will occur at $1 - p_c$, or just 44.4% area coverage of CNC assuming uniform coverage is achieved. For ultra-high aspect ratio particles such as silver nanowires, the percolation threshold is expected to be very low; in the case of 1 um long nanowires of 50 nm diameter, Eqn. (1) predicts a percolation threshold at just 26% of area covered. It is also useful to contrast CNC to the case of spherical particles, such as silver nanoparticle inks commonly used as printable conductors. The percolation threshold determined by Xia and Thorpe[21] for perfectly round particles can be reduced to the following relationship,

$$p_c = \frac{1}{3} \qquad (2)$$

and is independent of particle dimensions as $a = b$ for spheres. From Eqn. (2) the corresponding area coverage for spherical particles is thus 66.6% at the percolation threshold. The result points to a 22% decrease in the area that needs to be covered by CNC as compared to spherical particles in order to create a conductive network, implying much less material is required to form a conductive network.

Furthermore, for core-shell type materials such as CNC coated with conductive polymers, the amount of conductive material is even further reduced from the volume of the nanorod, approximated as a cylinder with volume $V_{filled} = L_{rod}\pi r_1^2$, where the length of the rod (L_{rod}) is the height of the cylinder, and the radius (r_1) is the radius of the rod, to just the nanorod shell, which can be approximated simply as $V_{hollow} = t_{shell}L_{rod}2\pi r_2$ where the thickness of the shell (t_{shell}) refers to the thickness of the conductive coating and the radius (r_2) refers to the bare CNC radius. Division of V_{filled} by V_{hollow} yields a reduction in volume by a factor of $r/2t_{shell}$ for cases where r = r_1 = r_2. The lower volume and area coverage needed allows for more efficient use of expensive conductive polymers or precious metals per surface area created, and is of great interest not only in printed conductors but also in catalysis and supercapacitor applications. For example, palladium nanoparticles coated on CNC nanocrystals by reduction of $PdCl_2$ salt were shown to be highly effective in hydrogenation and Heck coupling reactions; likewise gold nanoparticles

deposited between CNC and PDDA have been shown to significantly enhance the reaction rate of the 4-nitrophenol to 4-aminophenol reduction.[22]

2.6 Ink selection

In order to evaluate the potential of conductive cellulose-based materials for use in electronics or inkjet printing processing, they were first characterized by probing conductivity and morphology. These two aspects are important in printable conductive films; high conductivity is required for an electrical contact to function, while particle morphology is important for network formation as well as determining if particle suspensions can be printed, and surface roughness is a concern due to the potential for shorting a device. The conductivity study was meant to act as a screening test for materials before efforts were undertaken to formulate a specific type of CNC into a proper inkjet fluid. Drop casting was chosen as a simple method for depositing the materials unto substrates to perform the initial screening. Two-point probe across a sub-millimeter distance of material bridging two electrodes was chosen as the characterization method for conductivity. Conventional 4-point probe testing required a uniform thickness on the order of several millimeters, which was not attainable with drop-cast films. An annealing study was carried out to determine the effects of heat and solvent treatment on conductive CNC and shed light on whether a post-processing treatment similar to the annealing of silver nanoparticles would similarly improve the conductivity of CNC-based materials. The outcomes of these studies were used to identify the best candidate for formulation into an ink which would be integrated with proof-of-concept thin-film transistor devices.

2.6.1 Conductivity

Two-point probe methodology was used to characterize the conductivity of the CNC solutions as-received (~7 mg/mL in deionized water, 0.1 w% sodium dodecylbenzenesulfonate (SDBS) as stabilizer). The purpose of this study was to determine the top performers based on the conductivity of the novel CNC materials and assess any impact on performance that the addition of CNC may have had on the intrinsic properties of conductive materials.

 A thin film of each material was drop cast on top of a thermal SiO_2-coated silicon wafer with gold electrodes being deposited through thermal evaporation and patterned by liftoff. Pairs of electrodes were isolated and used to apply and sweep a bias while the current passing across the material was measured (Keithley 6430 and 2400) using custom-written LabView software.

By plotting the resulting I-V curve and extracting the resistance of the film from the slope, S, using the relationship in Eqn. (3):

$$R = \frac{\Delta V}{\Delta I} = \frac{1}{S} \qquad (3)$$

it is possible to calculate the resistivity, ρ, and its inverse, conductivity, σ, of a sample with known dimensions, using Eqn. (4):

$$\rho = t\frac{RW}{L} = \frac{1}{\sigma} \qquad (4)$$

where t is the thickness of the film, R is the measured resistance obtained from the slope of a current-voltage curve, and W and L are the width and distance between contacts, respectively. The schematic of this geometry can be seen in Figure 9.
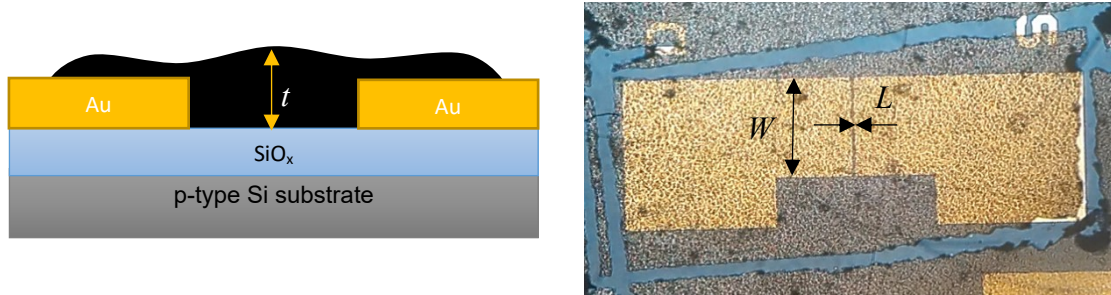
Figure 9 Schematic of drop cast CNC sample test structure (left), optical microscope image of CNC-AgNP cast on top of gold electrodes (right)

Profilometry (DEKTAK 8 model) was used to measure the thickness of the drop-cast films and the average value taken. Conductivity results are summarized in Table 1 below. Conductivity of bulk polypyrrole depends heavily on polymerization and processing conditions, ranging from as low as 10^{-3} S-cm^{-1} and up to 500 S-cm^{-1}.[15][23] All three forms of polypyrrole-modified CNC exhibited conductivity in the middle of this range. We determined that the polypyrrole-coated CNC inks pre-coated with PVP had the highest conductivity among the polymeric conductors tested,

being second only to Ag-NP functionalized CNC that showed approximately 2 times higher conductivity.

Table 1 Conductivity of drop-cast functionalized crystalline nanocellulose films.

Material	Resistivity [Ohm· m]	Conductivity [S· m⁻¹]	Appearance
CNC-PPY	0.18	5.60	Black liquid
CNC-PD-PPY	$7.22 \cdot 10^{-2}$	13.8	Black liquid
CNC-PEDOT:PTSA	$1.99 \cdot 10^{-2}$	50.3	Dark blue liquid
CNC-PEDOT:PSS	$1.33 \cdot 10^{-2}$	75.3	Dark blue liquid
CNC-PVP-PPY	$1.28 \cdot 10^{-2}$	77.8	Dark black liquid
CNC-AgNP	$6.85 \cdot 10^{-3}$	146	Brown-silver liquid

PEDOT materials cast from solution generally exhibit a conductivity on the order of ~1-100 S-cm⁻¹, although ultrahigh conductivity reaching 6400 S-cm⁻¹ has been reported by using specialized coating techniques such as solution-shearing.[24] When polymerized on cellulose nanocrystals both types of doped PEDOT performed poorly relative to the reported bulk conductivities. Attempts to improve the surface coverage of PEDOT on cellulose nanocrystals by pre-coating CNC with PVP as in the case of CNC-PVP-PPY yielded soft, gel-like films that showed insulating behaviour. Further work was not done to optimize the PEDOT synthesis process.

2.6.2 Morphology

Drop-cast films generally exhibited a matte, iridescent appearance typical of cellulose nanocrystal films when viewed under the optical microscope, indicating a textured surface with nano-scale roughness. Films of CNC-PPY-Ag appeared light brown, while films of CNC-PPY appeared black. The nanostructure of CNC-PVP-PPY was studied by tapping mode atomic force microscopy (Dimension 3100 AFM) and field-emission SEM (Leo 1550) in order to gain an understanding of how the cellulose nanocrystals are distributed in a thin film and an estimate of the surface roughness.
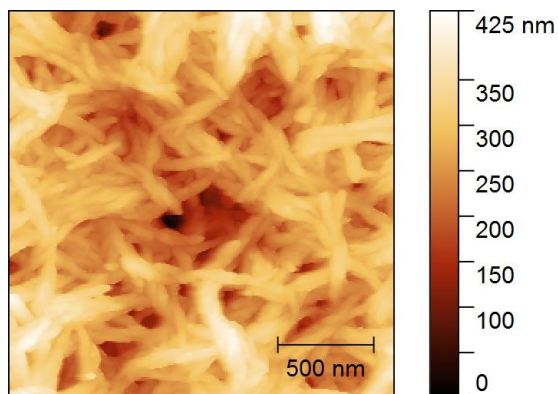
Figure 10 AFM topography mapping of printed NCC-PVP-PPY electrode.

CNC functionalized with PVP-PPY and drop-cast on SiO_2 is shown in an AFM image in Figure 10. The material presented a disordered, highly porous network with a surface root mean square (RMS) roughness of 59 nm (measured over an area of $4um^{2)}$ as determined by post-processing software Gwyddion. (http://www.gwyddion.net)
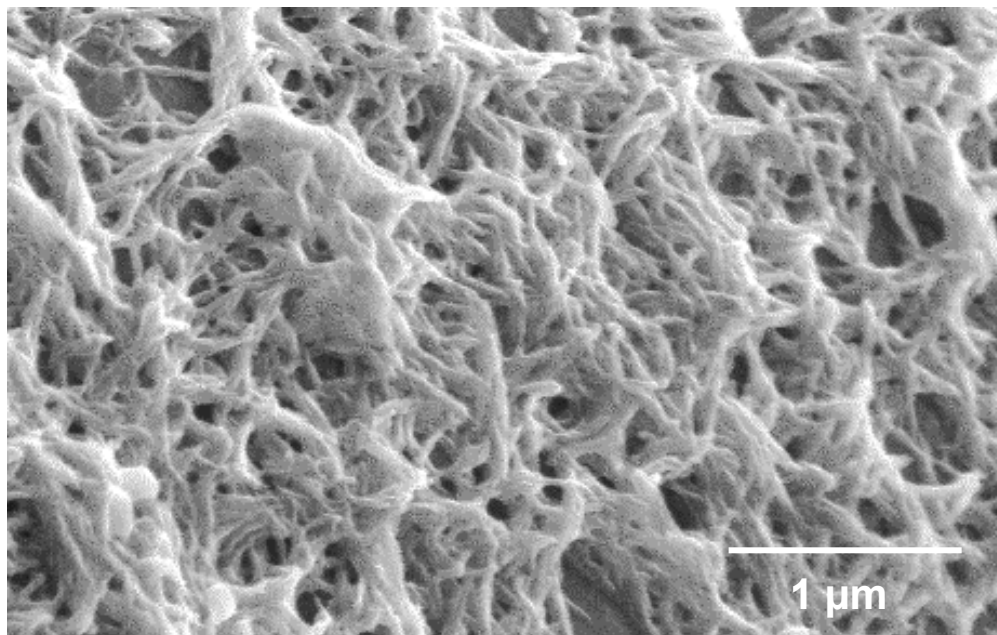
Figure 11 SEM image of drop-cast CNC-PVP-PPY, mounted on a 45 degree stub to show high porosity and surface texture.

Figure 11 was obtained by imaging the CNC film mounted on a 45-degree angle stub with SEM to obtain an idea of the in-plane morphology of the cellulose nanocrystal mesh. Together with Figure 10, these images show that much of the percolation network is void of conductive CNC material and provides insight as to why pressed pellets of PPY-coated CNC measured by Wu et al. (4.5 S-cm^{-1}) may have yielded a higher conductivity than that measured in this study (0.77 S-cm^{-1}). It is likely that the reduction of void space plays an important role in improving the effective conductivity, as the methodology used in this work reports on the overall 'bulk' conductivity of the unpressed 3D mat. From the pressed pellet versus free film conductivities for CNC-PVP-PPY we estimate that the void volume is approximately 80%. For further work it may be useful to investigate mechanical pressing or hot rolling as a post-processing technique to reduce void space and increase the bulk conductivity of CNC films; the technique has been shown to be highly effective at reducing surface roughness as well as improving conductivity of silver nanowire electrodes[25][26] and may be similarly applicable to conductive CNC.

2.6.3   Effect of Annealing

Heat treatment was investigated in order to determine whether thermal annealing is beneficial for the silver nanoparticle- and organic conductor-coated CNC materials. An annealing process is a well-known method used to improve the conductive paths between individual spherical silver nanoparticles by sintering and joining the individual particles together; this process occurs at temperatures far below the melting point of bulk silver in the case of nanoparticles due to size-dependent melting point depression.[27] A study was carried out based on this idea to determine if post-processing in the form of annealing is likewise required for the CNC materials. Thermal degradation studies using thermogravimetric analysis (TGA) have shown the onset of degradation for cellulose nanocrystals begins at 150°C with 20% of weight lost by 200°C.[28] This was confirmed with our own attempts to anneal conductive CNC at 200°C resulting in a significant drop in conductivity for all materials. The effect may be attributed to mass loss of cellulose nanocrystals at this high temperature, resulting in the subsequent loss of conductive pathways. Annealing at 150°C was chosen as an appropriate temperature for CNC-based materials to avoid degradation of CNC and loss of conductivity. Annealing was done in a laboratory oven (Blue M) in air for 20 minutes and the results have been summarized in Figure 12.
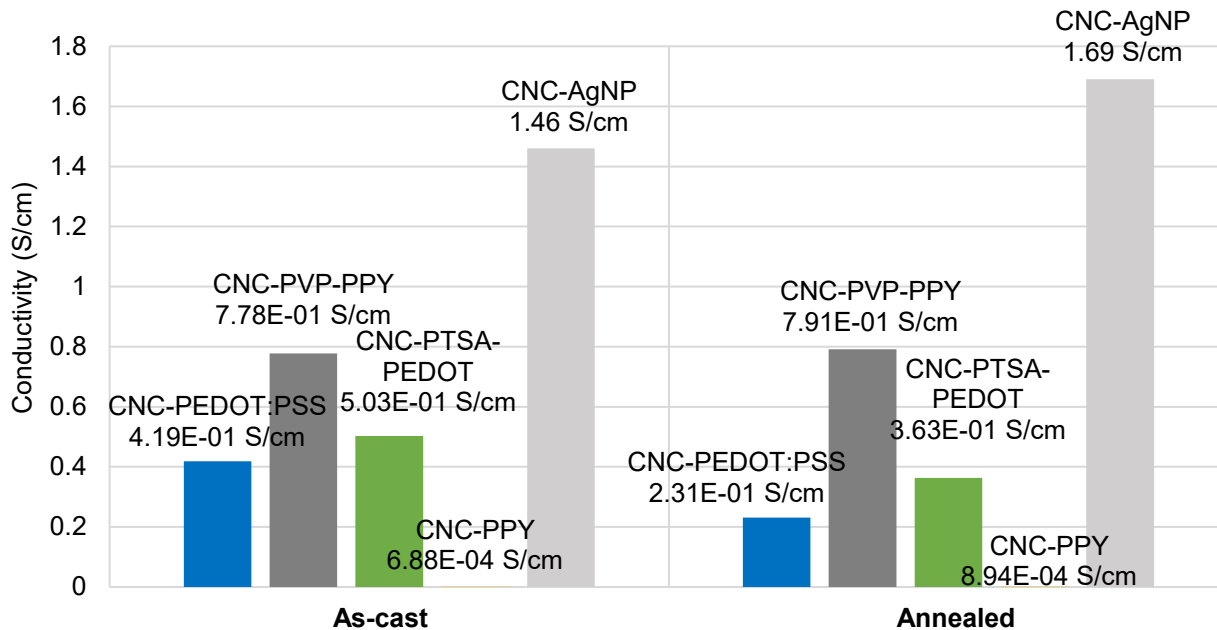
Figure 12 Effect of 20 minute 150°C heat annealing step on conductive CNC materials.

A minor improvement was seen in silver nanoparticle-coated CNC with conductivity improving by 15.7%; this effect is likely attributed to the sintering phenomenon previously described. The results also showcased the impressive stability of CNC-PPY and CNC-PVP-PPY. Conductivity of polypyrrole-coated samples increased very slightly with annealing, as contrasted with both PEDOT:PSS and PEDOT:PTSA functionalized CNC which suffered from a 1.4-1.8 fold reduction in conductivity.

Solvent annealing was briefly attempted during this study in order to improve the conductivity of polythiophene-functionalized CNC, as thermal annealing did not provide any improvement in conductivity. The Alcohol Vapor Treatment (AVT) method as described by Fallahzadeh et al. has been shown to create a two-fold increase in the conductivity of PEDOT polymer films. The basis of this technique is that increasing the mobility of polymer chains through exposure to a polar solvent can allow them to reorganize into separate grains of positively charged PEDOT and negatively charged PSS for improved carrier conduction.[29] The technique was tested on freshly prepared CNC-PEDOT:PTSA and CNC-PEDOT:PSS samples using methanol. AVT treatment consisted of exposure of the sample to methanol vapour by placing a covered glass petri dish with a small amount (~1mL) of methanol on a hotplate at 50°C to form an alcohol vapor. After twenty

minutes under AVT samples were removed and measured again for conductivity, however, no change was observed. It was concluded that AVT treatment with methanol using the procedure described does not improve conductivity of CNC-PEDOT materials. Grain sizes for PEDOT:PSS vary with processing conditions but have been reported on the order of tens to hundreds of nanometers.[30] Grain size may be the reason why solvent annealing did not improve conductivity; the PEDOT coating thickness on CNC is on the same order of magnitude as a typical PEDOT grain and thus the benefit in grain-to-grain conduction from solvent annealing treatment is unlikely to create the same improvement as seen in bulk films.

2.7 Summary

CNC nanoparticles with various conductive coatings were drop cast and tested between gold contacts for conductivity using the two-point probe method. The top performer out of all the materials tested was silver nanoparticle-functionalized CNC with a conductivity of 146 $S\text{-}m^{-1}$. Polypyrrole functionalized cellulose nanocrystals exhibited the second best conductivity overall, 77.8 $S\text{-}m^{-1}$, and better conductivity than two types of polythiophene-functionalized cellulose nanocrystals. Thermal annealing showed a drop in conductivity for PEDOT-functionalized CNC materials and a small increase in the conductivity of PPY- and Ag-NP-functionalized CNC. Solvent vapour treatment with methanol was not found to improve the conductivity of CNC materials functionalized with polythiophenes. Out of the five materials studied, CNC-PVP-PPY was chosen as an interesting option to move forward with for print processing due to its good environmental stability, conductivity, and simple synthesis in water without the need for solvents as compared to Ag-NP.

3 Printable Electronics

3.1 Inkjet Technology

At its core, inkjet printing is the generation of drops of liquid and their precise deposition on a substrate. Inkjet printing had its early beginnings in the discovery that fluids coming out of an orifice such as a tap or drain will spontaneously form droplets; this was first noted and described by Savart in the early 19th century. Later this effect was further investigated by Plateau and Rayleigh. Rayleigh built upon and summarized the linear capillary instability of jets which we now call the Rayleigh instability; any continuous thread of fluid is prone to break up into a form that minimizes the surface area of the fluid – a series of spheres – due to the amplification of tiny perturbations in the stream. This was built upon in the late 20th century to yield continuous inkjet printing- a technique that exploits the fundamental drive of liquids to minimize their surface area due to the force of surface tension, and redirects the droplets of ink unto paper in order to form an image. From this early start inkjet printing has expanded from graphics into the realms of medicine, electronics, nanomanufacturing and more. Inkjet printing can be used to manufacture small features by the precise placement of miniscule volumes of liquid inks which solidify and leave the desired deposit of material as the solvent evaporates. Other techniques such as temperature-catalyzed solidification or photoinitiated chemical reaction (e.g. ultraviolet (UV) curing) can be used to enhance this process. A significant benefit to this process is the ability to directly pattern and assemble features, requiring no masks, etching processes, chemicals, or other patterning steps associated with subtractive manufacturing. Subsequently, inkjet printing significantly reduces material waste, resulting in more cost-efficient manufacturing and use of materials.

The family of inkjet printing includes many systems which fall under the categories of continuous inkjet (CIJ) or drop-on-demand (DOD) inkjet. The family tree of these processes is shown in Figure 13. In both parent techniques, liquid drops with volumes from 0.5 to 500pL are ejected from a small orifice on the order of micrometers in diameter, with the difference being in whether this ejection is a continuous series of drops, as in the case of CIJ, or triggered, as in DOD inkjet. Continuous inkjet printing applies the trick of charging droplets as they are ejected; the droplets pass by plates that can also be charged, but with the opposite polarity. Controlling the charge at the plates allows the printer to deposit drops where they are required on a substrate, while

deflecting the ink into a recovery reservoir when passing over an area of the substrate that should remain blank. A significant advantage is consistency of droplet ejection, as the first several drops ejected by a DOD will have more variance in size, speed of flight, and angular deviations than later drops due to a 'priming' effect.
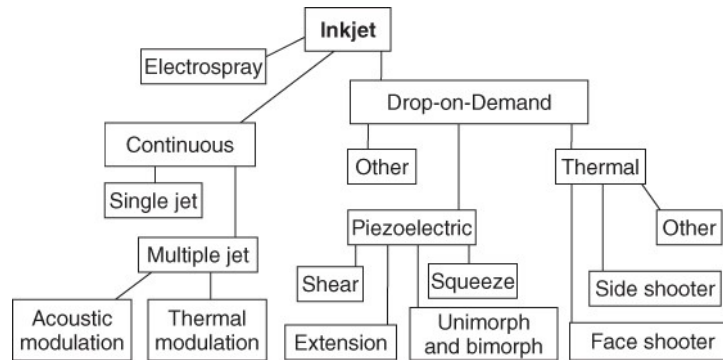
Figure 13 Classification of inkjet technologies.[31]

Inkjet printers now commonly found in homes and offices worldwide use a piezoelectric or thermal (colloquially termed 'bubble-jet') ejection mechanism. In the case of bubble-jet, a microbubble is generated by heating a filament or plate and thus bringing the surrounding ink into a gaseous state. The newly formed gas bubble increases pressure inside the printhead and pushes fluid out of the orifice. The main challenge often encountered in a bubble jet setup is clogging of the nozzle with particulates of ink that have degraded due to the spikes in temperature and pressure.[32] Piezoelectric printheads generally avoid this issue by using a piezoelectric element in order to generate and propagate an acoustic wave inside the fluid. By applying a positive or negative potential it is possible to contract and expand the piezoelectric material and create drop ejection 'on demand'.

The science of drop-on-demand inkjet has been extensively studied and described by groups such as Dong et al. in 2006 and Liu et al. in 2012. These studies have shown intuitive relationships including 1) drop diameter being proportional to nozzle orifice size, 2) an inverse relationship between drop volume and viscosity, and 3) an increase in printed line widths with higher piezoelectric driving voltage. Dong et al. have also developed models describing the different stages of the DOD jetting process.
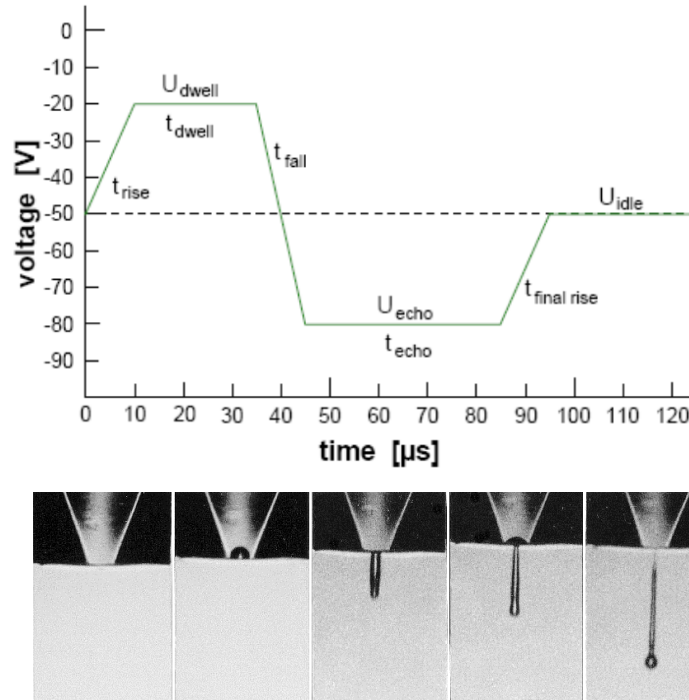
Figure 14 Jetting waveform typical of piezoelectric printheads (Microfab Inc.) and stroboscopic images of fluid being ejected from a piezoelectric printhead.

Ejection typically occurs in multiple stages as illustrated in Figure 14. Initially as a positive pulse is applied during t_{rise}, the piezoelectric element expands and the meniscus retracts into the orifice; next, this position is held during t_{dwell}, then followed by a sharp expulsion as the pulse is inverted during t_{fall} and fluid is pushed out; finally, ejection occurs during t_{echo} as the fluid forms a ball at the head of the jet and is cut off during t_{final} as the pulse is inverted one last time. As the fast-moving tail of the drop catches up to the main droplet it is possible to generate additional unwanted drops known as 'satellites'; satellite drops form when the tail is long enough such that it does not catch up to the main drop and instead gets pinched into smaller drops due to the Rayleigh instability.[33] A jetting waveform can take on multiple shapes depending on the properties of the ink being ejected; a denser fluid may require a stronger contraction or higher amplitude pulse, whereas a more viscous fluid will require longer dwell time for the wave to propagate to the orifice.

In this work two types of inkjet printheads, or dispensers, are used: glass-tipped 60μm single-nozzle piezoelectric inkjet dispensers from Microfab Technologies Inc. (Plano, TX) as pictured in

Figure 14, and a Dimatix 256-nozzle 30 picoliter Sapphire printhead. Both printheads were installed on a Ceradrop L-serie materials printer with ±2 µm X-Y stage resolution and controlled through CeraPrinter software. Microfab dispensers are comprised of a cylindrical reservoir encased in a radial polarized lead zirconate titanate (PZT) sleeve and were actuated using a JetDrive III pulse generator that was integrated into the Ceradrop L-series printer. In the case of the Dimatix printhead, the waveform generation was done directly through the printer hardware. Positive and negative pressure used to feed, purge, and control the meniscus of ink at the nozzle tip or nozzle plate was directly controlled through the CeraPrinter software.

3.2 Formulation development for inkjet printing

The use of inkjet printing for electronics applications requires an ink to possess electrical properties necessary for its respective role in the device being made, this can be conductivity, mobility, and low leakage current, while also satisfying the basic requirement of printability. This requirement is comprised of two needs. First, the ink must be capable of being printed with accuracy and repeatability in order to create desired patterns. Second, the ink has to have favourable physiochemical properties, including surface tension, viscosity, and boiling point, which allow for optimal jetting and enable one to deposit the desired materials with the required surface morphology. In this work, it was necessary to start from an aqueous base and develop an ink that could be used in a materials printer to deposit cellulose nanocrystal materials in an accurate and repeatable manner.

3.2.1 Influence of fluid properties on printing behaviour

Fluid properties will strongly influence many aspects of the printing process; the jetting behavior and how the fluid responds to the pressure wave generated inside the printhead, the final drop size on the substrate, as well as the likelihood of undesirable features forming, are all guided and predicted by fluid properties.

There are three processes fundamental to inkjet printing; first the generation of a pressure wave through mechanical deformation of the piezoelectric element and propagation to the nozzle opening; second, the retraction and expansion of the meniscus at the nozzle tip and the push of

fluid out of the nozzle; and finally, the instability of the fluid jet and drop formation. The jetting properties of inks corresponding to these processes can be assessed through the use of dimensionless groups; these are derived from fundamental properties including viscosity and surface tension, as well as jetting parameters such as the nozzle diameter and droplet velocity, to provide insight into what forces dominate the drop formation, ejection and spreading processes. There are three dimensionless numbers used for this purpose; the Reynold, Weber, and Ohensorg numbers.

The Reynolds number, N_{Re}, provides insight into the relative strength of inertial versus viscous forces in a fluid, and is defined as:

$$N_{Re} = \frac{\rho d V}{\eta}$$

(5)

where the density of the fluid is given by ρ, d is the diameter of the ejected drop, V is the velocity of the fluid, and η is the dynamic viscosity. Similarly the Weber number, N_{We}, tells us of the relative strength of the inertia of a fluid compared to the surface tension or capillary forces and is defined as:

$$N_{We} = \frac{\rho d V^2}{\sigma}$$

(6)

where the surface tension of the fluid is σ. The behaviour of the ink on the substrate, or spreading behaviour, can be determined from these two hydrodynamic properties.[34] In general these two equations can be taken to imply that a fluid with high Weber or Reynold numbers will also tend to spread more upon impact and create thicker traces.

As the velocity of drops is tied to printing speed and distance from a substrate -normally fixed in a printing system- it is possible to remove the influence of jetting parameters by combining the Re and We numbers into another dimensionless group, the Ohnesorge number, N_{Oh}, which is defined as:

$$N_{Oh} = \frac{\sqrt{N_{We}}}{N_{Re}} = \frac{\eta}{\sqrt{\sigma \rho d}} \qquad (7)$$

The Ohnesorg number reflects the physical properties of a jet of fluid (surface tension, viscosity) exiting a nozzle as well as the scale on which the jetting is taking place through the characteristic length, while removing the influence of jetting conditions (velocity). A high Ohnesorge number (Oh >~1) thus reflects a fluid governed by viscous forces that act to prevent the separation of the fluid and impede drop formation; on the opposite end, a low Ohnesorge number (Oh <~0.1) results in strong surface tension forces that split up a jet into multiple drops, resulting in unwanted satellite droplets. It is thus a commonly utilized number for outlining the useful operating range of inkjet printing and predicting the jetabbility of new inks in development by a simple calculation; fluids with Ohnesorge numbers falling into the category of 0.1 < Oh < 1 should in theory be jettable. Another commonly used form of this dimensionless number is Fromm's parameter Z, the inverse of the Ohnesorge number ($Z = \frac{1}{Oh}$).

A recommended jettable range determined by Reis et al. through numerical simulation was found to be 10 > Z > 1. The predicted printability zone is graphically summarized by McKinley and Renardy in Figure 15. Several constraints to printability are shown in the figure below; a drop with sufficient kinetic energy to be ejected from the nozzle has $N_{We} \geq 4$ or $N_{Re} \leq 2/N_{Oh}$, defining the left-most limit for N_{Re}; conversely, splashing occurs after $N_{Oh}N_{Re}^{5/4} \geq 50$ and creates undesired extra drops, defining the right-most limit of the zone.[35] Jang et al. later redefined the optimal range to be 14 > Z > 4 by inkjet printing mixtures of ethanol, water, glycerol, ethylene glycol, and diethylene gycol mixtures. Though inks with Z < 4 are wholly possible to print, it takes a longer time to generate one droplet which in turn requires a large distance between the substrate and the printhead and amplifies drop positioning errors.[36]
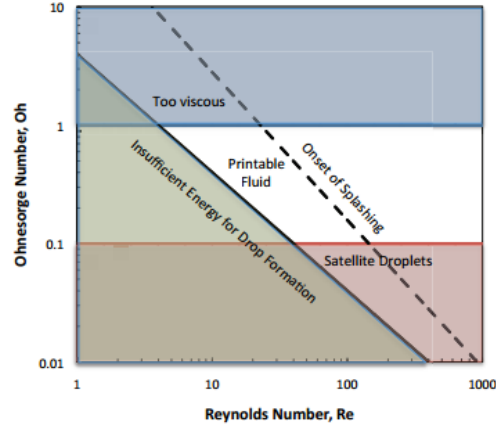
Figure 15 Schematic showing regimes for DOD inkjet printing. (Mckinley & Renardy, 2011)

Finally, the model developed by Asai et al.[37] can be used to predict the ratio of the final drop diameter on the substrate, D_{max}, to free drop diameter, d. The model does not take into account more complex phenomena due to surface energy or roughness of the substrate but has been shown to serve as a good approximation of D_{max}. An upper limit on d is provided by the inkjet nozzle orifice diameter as the droplet diameter will rarely be greater than the nozzle. By using the Asai model we can predict the maximum size of a jetted drop or conductive line in a simple manner from known or easily attainable properties of the system.

$$\frac{D_{max}}{d_0} = 1 + 0.48We^{\frac{1}{2}}\exp[-1.48We^{0.22}Re^{-0.21}]$$ (8)

3.4 Developing printable CNC inks

In this work we tuned the fluid properties, CNC concentration and jetting waveforms to arrive at an ideal suspension of cellulose nanocrystals. The work done was pivotal to the ability to accurately deposit this novel material. Starting with the guidelines for printability previously outlined and a stock of CNC nanoparticles suspended in water, it became evident from calculation of the Weber, Reynolds, and Ohnesorge numbers that the surface tension of the final ink formulation would likely need to be reduced and the viscos

ity increased. The surface tension of pure water, 72.8 mN-m, and viscosity, 1.002×10^{-3} Pa-s, printed using a nozzle size of 60 microns and a drop velocity of 1.5 m/s, was used to calculate the dimensionless numbers summarized in

Table 2 and compared with two other fluids commonly used in aqueous inkjet inks: ethanol and ethylene glycol. In Figure 15 pure water is located below the printable zone with an Ohnesorge number of 0.02 and Reynolds number of 89.6. The Z number of 65.8 is subsequently also non-ideal.

Table 2 Dimensionless numbers for three common solvents jetted at 1.5 m/s with a nozzle orifice of 60 μm.

	ρ kg/m³	η, 20°C mPa-s	σ, 20°C mN-m	N_{Re}	N_{We}	N_{Oh}	Z
Water	998	1.00	72.75	89.57	1.85	0.02	65.81
Ethanol	780	1.25	22.31	61.36	4.72	0.04	28.25
Ethylene Glycol	1113	19.8	48.4	5.05	3.10	0.35	2.87

In order to increase N_{Oh} and land within the printable range of $1 > N_{Oh} > 0.1$, there are two potential solutions. The first solution plays on the role of the dimensions of the jetting orifice; by decreasing the nozzle size we can increase the Ohnesorge number. This approach is often non-ideal as the nozzle size in a printing system is not always possible to change; in the case of nanoparticle inks

lowering nozzle size could also be undesirable as a smaller nozzle may increase the likelihood of clogging. The second, and more preferred, approach is by taking advantage of the roles of fluid properties in order to tune the ink. Eqn. (7) tells us that several options exist: a decrease in surface tension, an increase in viscosity, or a decrease in density will all increase N_{Oh}. Surface tension can be lowered by addition of a compatible solvent such as ethanol; alcohols are good candidates as they possess surface tensions in the range of 20-30 mN-m as well as favorable solubility with water and nanocrystalline cellulose. Experimentally determined values for surface tensions of binary mixtures of water and ethanol are shown in Table 3.

Table 3 Surface tension of binary ethanol-water mixtures measured empirically and reported by Gonzalez et al.[38]

Ethanol (w/w) %	Surface Tension, 20°C mN-m
0	72.75
10	48.14
20	38.56
30	33.53
40	30.69
50	28.51
60	26.72
70	25.48
80	24.32
90	23.23
100	22.31

From Table 3, it is clear that although it is possible to control the surface tension of an ink very carefully within the range of 22 to 72 mN-m by varying the ratio of two solvents, ultimately this results in less than an order of magnitude in the change of the Ohnesorge number. It follows that an ideal N_{Oh} cannot be achieved solely by applying this approach. In addition to this method of increasing the Ohnesorge number we can alter the viscosity of the ink. Common additives used to increase the viscosity of aqueous inks include the family of glycols (ethylene, diethylene, etc.) and their polymerized forms (poly(ethylene glycol), etc.) Dynamic viscosity values for a binary mixture of ethylene glycol and water determined experimentally by Bohne et al. as well as Jang et al. can be seen in Table 4.

Table 4 Dynamic viscosity of ethylene glycol–water binary mixtures at 20 C reported by Bohne et al.[39] and Jang et al.[36]

Ethylene glycol (w/w) %	Bohne et al. Viscosity, 20°C mPa-s	Ethylene glycol (w/w) %	Jang et al. Viscosity mPa-s
100	22.40	77	12.3
74	8.14	53	7.61
50	3.72	27	3.69
25	1.87	16	3.11
0	1.00		

There are several options for predicting the viscosity of a binary, ternary, or even more complex mixture. The simplest form is a mole-fraction weighted expression such as the one shown for binary mixtures in Eqn. (9),[40] the shape of which mimics the natural exponential form of experimental data and passes through the boundary conditions at 0% and 100% mole fractions X_1 and X_2 at which viscosities correspond to those of the pure liquids.

Here we make the assumption that the dynamic viscosity (η) of a mixture is a simple function of mole fraction ($X_1, X_2 \dots X_i$) and the dynamic viscosity ($\eta_1, \eta_2 \dots \eta_i$) of the individual components,

$$\ln \eta = X_1 \ln \eta_1 + X_2 \ln \eta_2 \tag{9}$$

Eqn. (9) can be extended to any number of components by summing up the product of each component's mole fraction and the natural logarithm of that component's corresponding viscosity:

$$\ln \eta = \sum_i X_i \ln n_i \tag{10}$$

For mixtures with ethanol, ethylene glycol, and water it was predicted that we can obtain a range of ink formulations with the viscosities and densities calculated and summarized in Table 5.

Table 5 Calculated viscosity and density of ternary mixtures with varying ratio of water-ethylene glycol-ethanol

Volumetric ratio	Predicted dynamic viscosity (cP)	Density (g/cm³)
3:1:1	1.335	0.978
2:1:1	1.489	0.972
1:1:1	1.902	0.964
1:1:0.6	1.982	0.992
1:0.6:1	1.537	0.941
0.6:1:1	2.344	0.958

In this work we were not able to gain access to equipment in order to experimentally measure the viscosity of the CNC-containing ink mixtures to validate this data. However, literature on aqueous CNC suspensions shows a clear increase in viscosity due to the presence of CNC, with suspensions of 1.9% (w/w) showing a relatively high dynamic viscosity between 30 to 200 mPa-s with a dependence of dynamic viscosity on shear rate.[41] To illustrate the effect of this property on the development of printable inks we may observe that the viscosity increase from the addition of 1.9% (w/w) of CNC would increase the dynamic viscosity of water to more than that of pure ethylene glycol. From an ink formulation standpoint, the complex viscous behaviour of CNC suspensions complicates analysis based on dimensionless groups, and furthermore the shear experienced by the ink during the jetting process may vary with the amplitude and frequency of the jetting waveform.

Moreover, formulations with CNC concentrations above ~1% (w/w) were not found to be printable through trial and error as materials would form a clog in the nozzle. For this reason, 0.5% (w/w) was chosen as the concentration of CNC particles for all subsequent formulations. The question was raised if the particle size to nozzle ratio exceeded the general guideline of nozzle size being greater than 100 times the particle size[42] (a 60μm nozzle such as the one used in this work requires a particle size of 600nm or less) however, this was not the case for the CNC inks used as seen from discussion of particle morphology previously. Clog-forming behaviour may be explained by the unique characteristics of monocrystalline cellulose suspensions; at low concentrations, aqueous suspensions of CNC form an isotropic randomly oriented phase, while above a certain concentration they form anisotropic chiral nematic liquid-crystal domains. The critical concentration is a function of the aspect ratio, charge density and osmolarity, and typically

ranges between 1-10% (w/w),[5] in agreement with the onset of clogging behavior seen in this study. This behavior is postulated to result from the CNC's high affinity for stacking due to hydrogen-bonding between cellulosic hydroxyl groups and oxygen atoms present in the CNC chains. An interesting concept that is postulated but not explored in this study is the potential for electrolytes (e.g. salts, polymeric electrolytes, etc.) to shield hydrogen bonding groups and disrupt stacking behavior with the goal of increasing CNC solids loading in inks while avoiding clogging. If electrolyte shielding is a viable technique for modifying inter-particle interactions between cellulose nanocrystals, it may also be a useful variable for tuning the viscosity and achieving desirable jetting characteristics in CNC inks.

In order to address the issues raised, a ladder test was carried out with various volumetric ratios of water, ethylene glycol, and ethanol to experimentally test jetting of ternary mixtures of CNC using a Microfab 60μm printhead jetting at 400Hz with a simple bipolar waveform. The amplitude, rise, dwell, fall, and echo times were tuned to best jet each ink. Good jetting behaviour was characterized by the following observations; formation of a stable meniscus at the jetting orifice, good response to applied waveform (<80V in amplitude) with expulsion of a 'necked' drop, ability of the drop to overcome viscous and capillary forces and separate from the neck, relatively fast velocity (>0.5m/s) of the expulsed drop, and a flight path with minimal angular deviation.

In contrast, inks with poor jetting behaviour exhibited one of more of the following: poor meniscus control, often wetting the nozzle exterior easily and impeding drop formation, low response to amplitude of driving waveform (necessary to increase amplitude to 90+V) or complete inability to overcome the surface tension of the fluid in order to form a necked drop, low velocity resulting in interaction with ambient air currents and drop 'disappearance' in which jetting occurs but no drop is present on the substrate, and finally, high angular deviation resulting in inconsistent drop placement.

Testing a variety of volumetric ratios for the ink components yielded an optimal ratio of 1:0.6:1 of water/ethylene glycol/ethanol, corresponding to 41/27/32 (w/w) %, to work well for consistent jetting while keeping the amount of ethylene glycol low enough that drying was not impeded and the concentration of nanoparticles was high enough to deposit a usable amount of material per drop.
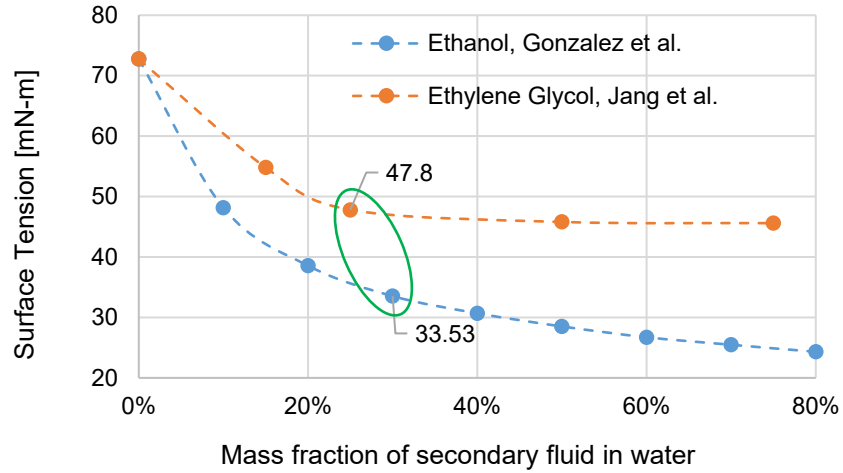
Figure 16 Experimentally determined surface tension for ethanol-water and ethylene glycol-water binary mixtures.

From theory the optimal ratio of fluids found through experimental printing studies corresponds to a surface tension of approximately 40 mN-m (estimated through interpolation between surface tensions of water-ethanol and water-ethylene glycol binary mixtures shown in Figure 16, a density of 941 kg/m^3, and a predicted viscosity of 1.537 cP as described previously. The ink formulation can be seen in various stages of printing in Figure 17.
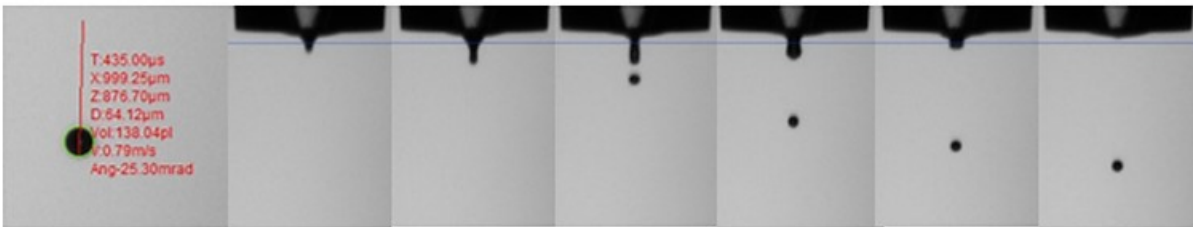
Figure 17 Ink dispending stages of printing CNC-PPY-Ag from aqueous ink and droplet characteristics showing ~54 μm diameter drops.

3.5 Drop formation and drying phenomena

Substrate-ink interactions due to printing parameters, surface energies and physical ink properties comprise a crucial component of the inkjet printing process. After droplet ejection, line width and layer topology is purely determined by the wetting and drying processes that occur when a drop hits the substrate. The surface energy of the substrate, or hydrophilicity, results in high fluid wetting and larger spread droplet size for high-energy surfaces, and likewise low wetting of lower energy surfaces creates smaller droplets and lines that spread less. In a system at equilibrium, this behavior is described through Young's relationship[43] which relates the contact angle θ of a liquid drop on a solid to the interfacial forces at the liquid-vapour (γ_{LV}), solid-vapour (γ_{SV}), and liquid-solid (γ_{SL}) interfaces:

$$\gamma_{SV} - \gamma_{SL} - \gamma_{LV}cos\theta = 0 \tag{11}$$

There are various undesirable phenomena that may occur during the formation of a still-wet printed feature; two notable effects are bulging (seen in printed lines) and the coffee stain effect (seen in individual drops).
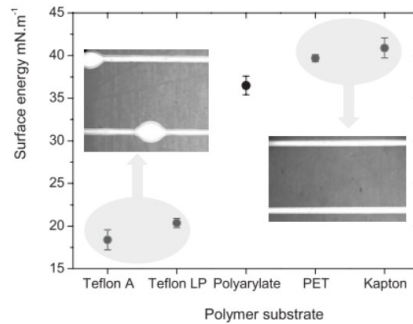
Figure 18 Surface energies of common commercially-available polymer substrates.[44]

Bulging is a regime where printed lines will form regular 'bulges' in the line due to the fluid's drive to minimize surface area that result in wicking of ink from the drop landing site into the line of previously deposited ink, shown in Figure 18. This is a regime occurring in a certain range defined by the printing frequency and drop overlap which is highly fluid and substrate surface

energy dependent.[44] Printing frequency determines how much time the fluid of each printed drop has to react to the substrate surface before the next droplet lands and effectively 'equalizes' the drive for wicking into the previous drop. High drop overlap increases the risk of bulging as there is less liquid-substrate interface being created per drop to effectively 'lock' the drop in place.

Bulging can be minimized in various ways; using a higher surface energy substrate (Figure 18) increases the favorable interactions between substrate and fluid to minimize beading up and wicking into previously deposited drops, and heating the substrate stage solidifies the ink and prevents ink from bulging. Another solution is to increase the spreading character of the ink, or effectively lower the surface tension of the fluid-air interface in Young's equation, as this will likewise reduce the chances of beading and bulging. For this purpose, low-surface tension fluids, e.g. alcohols, and additives, such as surfactants, are often used to improve wetting behaviour by lowering an ink's surface tension to fit the range of 30-40 mN-m.
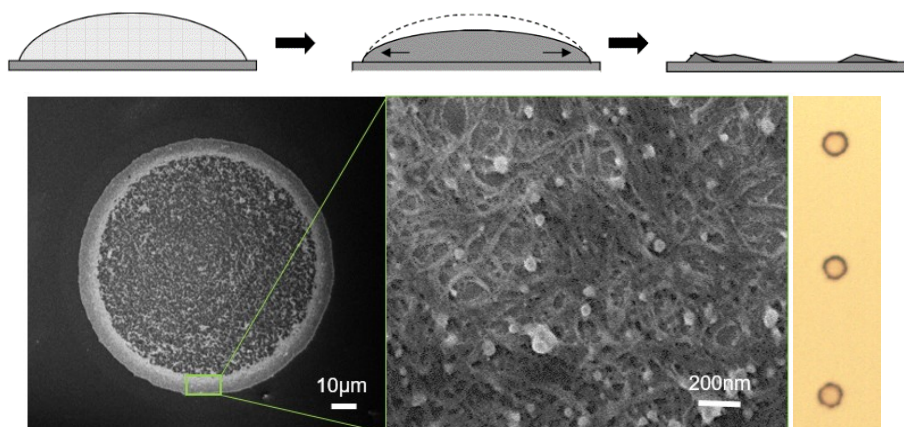
Figure 19 Top: mechanism of coffee stain effect, bottom left: SEM image of first attempts to print CNC-Ag stock on silicon nitride, the drop shown exhibited a strong coffee stain effect. Middle: Magnified view of nanoparticle network. Right: optical microscope view of the printed droplets.

The coffee stain effect is an infamous undesirable effect that is often encountered in inkjet printing. A droplet with a pinned perimeter will evaporate across its whole surface and its subsequent thickness will decrease- however, for the contact line to stay pinned in place, the loss of volume at the perimeter will require a net outward convective flow in order to maintain the contact

boundary.[45] For a particle-loaded fluid this flow moves material from the middle and deposits it in a ring on the drop perimeter as seen in Figure 19 to form a classic 'coffee-ring' appearance.

In single-solvent ink systems (such as the aqueous suspension of CNC-AgNP shown in Figure 19), the coffee stain effect results in multiple negative effects. A large discrepancy in the printed drop profile, with high film roughness and non-uniform distribution of material, will have a negative impact on electronics devices due to pinholes, shorts, and inconsistent layer thicknesses. A common strategy used to mitigate the coffee stain phenomenon is to induce a convective recirculative flow within the drop known as Marangoni flow. Majumder et al. showed that aqueous nanoparticle solutions could be dried into uniform films while avoiding the coffee ring phenomena by allowing the film to dry under an ethanol vapor environment. This generates a surface tension gradient which drives recirculating flow as demonstrated in Figure 20, from regions of high tension to low tension. This flow is similar to that seen in the phenomenon of 'wine tears' where wine will move up the inside of a wine glass due to the evaporation of ethanol and a subsequent ethanol vapour forming at the surface of the liquid.
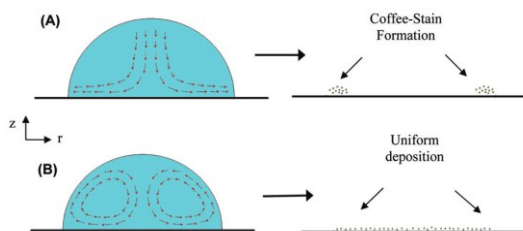
Figure 20 Schematic of convection within a printed drop during (a) coffee stain formation, and (b) uniform drying with Marangoni flow. (Majumder et al. 2012)

A simpler solution to the coffee stain phenomena can be implemented through addition of a secondary solvent which possesses a different boiling point to that of the original fluid. When an ink is comprised of a mixture of a low and high boiling point solvents, the relative concentration of solvent at the contact line -where the evaporation rate is higher- will be skewed towards the higher boiling point solvent; as such, the rate of evaporation at the contact line is slowed, and a surface tension gradient is established across the drop, causing a flow from regions of low surface tension to high surface tension. As demonstrated by Gans et al. the concertation gradient does not

have to be significant to start the process of Marangoni flow in order to homogenize the drop composition and allow for uniform drying.[46]
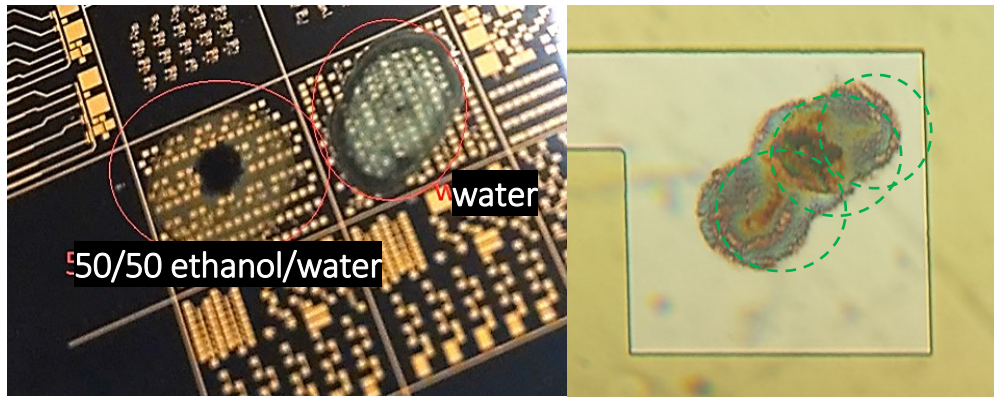
Figure 21 Left: Drop-cast CNC-PPY stock ink (water) and mixed 50:50 with ethanol showing inhibition of coffee stain effect, right: three jetted CNC-PPY droplets, using ink formulated with both ethanol and ethylene glycol showing uniform material deposition and drying.

As can be seen in Figure 21, CNC-PPY stock solution (before formulation, left image) showed a significant coffee stain effect. By adding an equivalent amount of ethanol to the stock, the drop dried more uniformly, though there was a thicker deposit left in the center of the drop. This effect was observed to be due to the ethanol-water mixture drying too quickly and losing the contact edge pinning. Addition of ethylene glycol (after formulation and printing, right image) served to fix this issue by reducing the drying speed and allowing for the drop contact edge to remain pinned. In Figure 21 multiple overlapping drops are shown on an n+ a:Si:H contact, with each individual drop showing material is uniformly deposited with no coffee ring effect or collection of material in the center.

Apart from the considerations for printability, the reason the CNC ink formulation developed worked well had to do with the combination of the two solvents we chose and their respective contributions to the droplet drying process. First, ethanol acted as both a lower boiling point solvent to complement ethylene glycol and water in order to set up a recirculating flow, and as a surface tension reducer for improved droplet wetting on a-Si:H. Second, ethylene glycol was used to raise the ink viscosity, aid in Marangoni convection, and slow down drying to prevent inverse-

coffee stain effects. This approach underlines the importance of optimizing ink formulation for both the jetting and the drop drying processes.

3.6 **Summary**

The work described above was carried out to determine the optimal marriage of parameters such as surface tension, viscosity, concentration of CNC, and how this related to drying phenomena for the purpose of creating the first jettable crystalline nano-cellulose inks. The prime result of this work are CNC inks that can be jetted reliably and with good accuracy, exhibiting markedly reduced coffee ring effect without compromised drying. The formulation developed is summarized in the table below with predicted fluid parameters and calculated dimensionless groups.

Table 6 Formulation and dimensionless groups for CNC ink.

	Volume ratio	w/w	ρ kg/m^3	η, 20°C mPa-s	σ, 20°C mN-m	N_{Re}	N_{We}	N_{Oh}	Z
CNC	-	0.5%							
Ethanol	1	32%	940	1.54	~40	54.94	3.63	0.035	28.85
Water	1	41%							
Ethylene glycol	0.6	27%							

It is important to note that CNC present at 0.5% (w/w) concentration is not accounted for in predicted values. In practice, due to the thixotropic nature of CNC suspensions it was determined that ink viscosity could not be predicted accurately; however, it is a likely reason for the good jetting performance of the inks despite the non-optimal values of dimensionless groups predicted for the specific solvent mixture. If we assume printability was satisfied (i.e. $4 < Z < 14$ and the associated Reynolds number is such that the ink is within the printable zone), the effective dynamic viscosity during printing must land within the range of 4-11 mPa-s. From an ink development standpoint this behaviour proves to be an interesting hurdle to incorporating CNC into jettable inks as fluid properties, particularly viscosity, are not trivial to predict for CNC systems and must be tested experimentally where additional systematic studies beyond the scope of this thesis are required.

4 Amorphous Silicon Thin-film Transistors

Thin-film transistors (TFTs) are commonly used devices in the flat panel display industry; they are also the most straightforward candidates for flexible and transparent electronics applications, with a-Si:H TFTs already demonstrated in large-area and inkjet printing applications. Additionally, a-Si:H is relatively stable at ambient conditions when kept in a controlled environment, allowing a window of opportunity for ambient processing such as inkjet printing. As such, a-Si:H TFTs were a natural choice for integration with novel printed contacts in order to create proof of concept devices using a nanocrystalline cellulose-based ink.

Three sets of devices were made in order to benchmark the pPy-NCC contacts: conventional devices with sputtered aluminum-chromium source and drain used as an intermediate step, devices with printed contacts using commercially available silver nanoparticle ink for comparison, and devices with printed CNC-PVP-PPY contacts. In this section we will discuss the operation, fabrication, and results from characterization of these devices.

4.1 Operation of a-Si:H TFTs

Thin film transistors require at least three materials, 1) a conductor to form the gate, source and drain contacts, 2) a dielectric to insulate the gate from the channel, and 3) a semiconducting channel material whose conductivity can be modulated with the application of an electric field. The most common materials system for thin film transistors used in large area applications, such as displays, is the amorphous hydrogenated silicon (a-Si:H) and silicon nitride (SiN:H) system, as both of these materials can be processed at relatively low temperatures from source gasses such as silane (SiH_4) and ammonia (NH_3), respectively, using large area plasma enhanced chemical vapor deposition (PECVD). Unlike crystalline silicon, in a disordered system the silicon forms randomly ordered bonds with its neighbours leaving some bonds unsatisfied and resulting in an amorphous material. Hydrogenation from the presence of hydrogen in the source gasses acts to stabilize unsatisfied dangling bonds in the amorphous silicon by termination with hydrogen. This creates a relatively stable amorphous semiconductor.

a-Si:H thin-film transistors operate as accumulation-mode field-effect transistor (FET) devices. In the 'Off' state, the intrinsically low conductivity of the amorphous material results in a very low but measurable off current, I_{OFF}. In the 'On' state, a conductive channel is created from charge accumulated at the channel-insulator interface upon the application of a gate bias, V_G, which allows carriers to flow between the source and drain, I_{DS}. There is an intrinsic threshold voltage, V_T, above which the transistor is considered to be 'On' and further increase in gate voltage yields diminishing increase in I_{DS}. () During operation, a potential is applied across the source and drain electrodes (VDS) which acts to sweep carriers through the channel. The operation is similar to the metal oxide semiconductor field effect transistor (MOSFET) operation in accumulation mode and is often modelled as such.
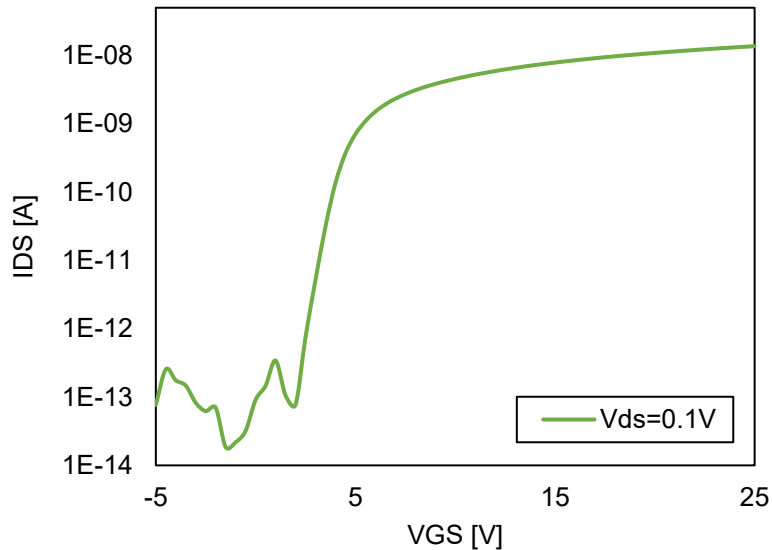
Figure 22 Transfer characteristics of a bottom gate W/L = 200 um/100 um n-channel a-Si:H TFT with V_{DS} = 0.1 V.
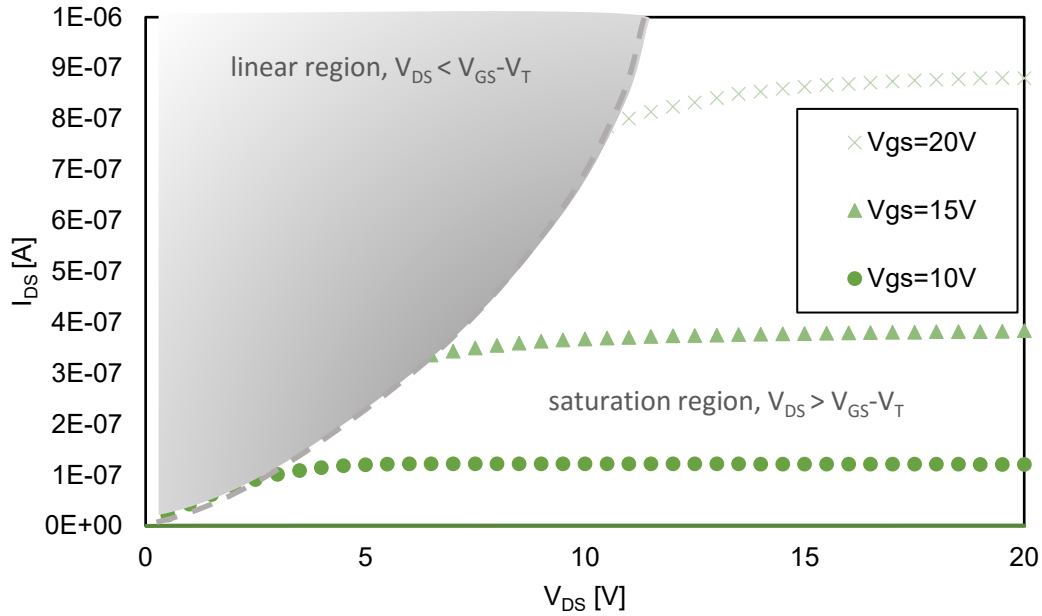
Figure 23 Output characteristics of I$_{DS}$ versus V$_{DS}$ for a fabricated bottom gate a-Si:H TFT with Al/Cr contacts and channel W/L=200/100μm.

There are two modes of operation for TFTs as illustrated in Figure 23: the linear regime where V$_{DS}$ is less than the overdrive voltage, V$_{GS}$ – V$_T$, and in the saturation regime where current through the device hits a maximum and saturates once V$_{DS}$ is greater than the overdrive voltage, as shown in Eqn. 12 and 13:

$$I_{DS_{lin}} = C_{ox}\mu_{FE}\frac{W}{L}\left[(V_{GS} - V_T)V_{DS} - \frac{V_{DS}^2}{2}\right], \qquad V_{DS} < V_{GS} - V_T \qquad \textbf{(12)}$$

$$I_{DS_{sat}} = C_{ox}\mu_{FE}\frac{W}{L}\frac{(V_{GS} - V_t)^2}{2}, \qquad V_{DS} > V_{GS} - V_T \qquad \textbf{(13)}$$

W and L are the respective width and length of the device channel, μ_{FE} is the field effect mobility of carriers in the device, and C_{ox} is the capacitance per area of the dielectric layer separating the channel and gate. The behavior described by these two equations is seen in output (I$_{DS}$ versus V$_{DS}$)

and transfer (I_{DS} versus V_{GS}) curves. and Figure 23 demonstrate such output and transfer plots obtained from fabricating an a-Si:H transistor with a bottom gate configuration as will be described in Section 4.2.

4.2 **Architecture and processing**
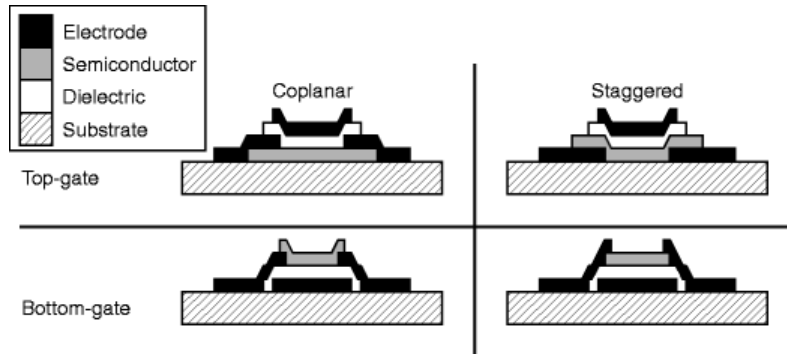
Figure 24 Cut schematic of four possible a-Si:H TFT architectures

In this work a-Si:H devices were designed with a common bottom-gate staggered architecture (Figure 24) to simplify processing, in which multiple devices shared one continuous gate provided by a highly doped p+ silicon substrate. The mask-set and process was developed as an adaptation from a 5 mask 3-inch a-Si:H TFT process commonly used by the Advanced Flexible Electronics Technology (AFET) research group in the Giga-to-Nanoelectronics Lab at University of Waterloo. A thermally grown 200nm of SiO_2 and 100nm of PECVD-deposited SiN:H formed a bilayer-dielectric to provide a high quality surface for the a-Si:H to grow on and reduce the amount of interface defects. 150nm of PECVD-deposited a-Si:H was grown on top of the dielectric stack to create a semiconducting channel, followed by a 50nm layer of phosphorous-doped a-Si:H. An n+ doped a-Si:H layer was deposited in order to create an ohmic contact between metallic source/drain contacts and the a-Si:H channel. Finally, approximately 100nm of aluminum and chromium were sputtered to form the source and drain contact layer and conclude the TFT layer stack, as shown in Figure 25.
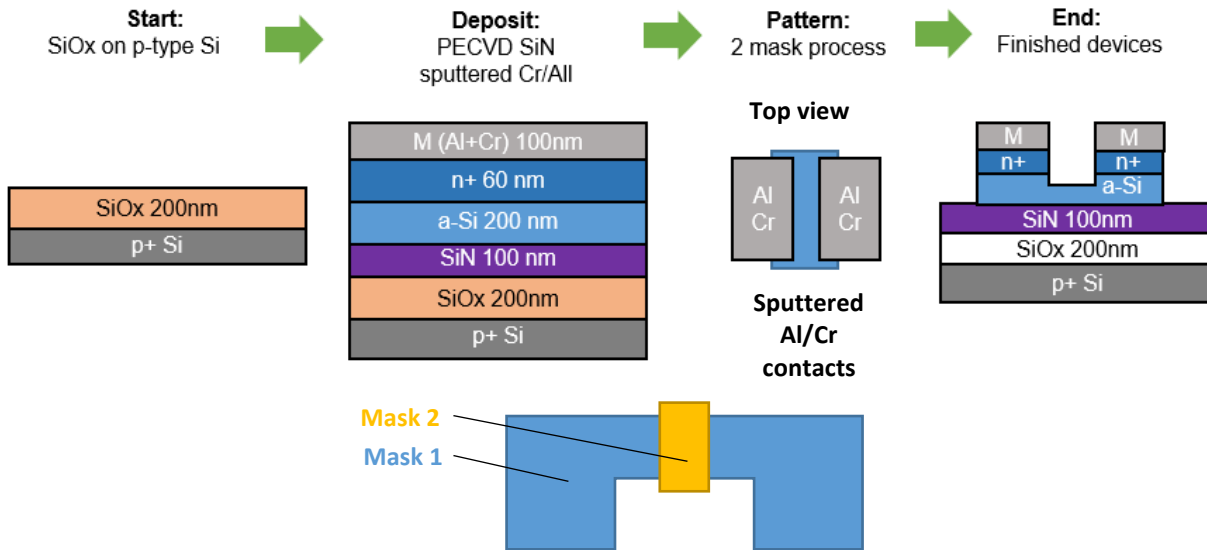
Figure 25 a-Si:H TFT fabrication process and cross-section schematic of devices.

The devices were then patterned using a simplified two-mask process developed in order to minimize the amount of processing required. First, the source and drain regions were patterned using photolithography and the sputtered metal layer was wet etched using Cr and phosphoric-acetic-nitric acid (PAN) etch to remove chromium and aluminum in regions around the source and drain, exposing the underlying n+ a-Si:H while protecting the contact areas. Photoresist was removed by soaking in acetone followed by isopropyl alcohol and DI water rinse before being blow-dried with dry nitrogen gas. Next, the channels were patterned using the second mask and reactive ion (RIE) dry etching (Phantom II Reactive-Ion Etching system, Trion Technology Inc.) with CF_4 gas used to etch a-Si:H n+ and a-Si:H layers to isolate the individual channel regions. The source and drain contact areas remained un-etched due to the sputtered metal effectively acting as an etch-resist. Finally, photoresist was stripped from the channels and a second RIE etch was done to remove the 50nm of n+ a-Si:H on the channel region with an over-etch of 50nm into the a-Si:H confirmed by profilometry. This process produced devices with a common gate and isolated channel regions as shown in Figure 25.

4.3 **Extracting transistor parameters**

There are several key parameters commonly reported which are used to determine transistor performance: field-effect mobility tells us how well injected carriers transport through the active

region of the device and is a figure-of-merit that describes how well the TFT can switch between on and off states; the threshold voltage, V_T, is the point at which the accumulation of charge within the channel region has overcome the density of defect states in the disordered semiconductor, creating a conductive channel for charge transport; the I_{ON}/I_{OFF} ratio demonstrates the difference between the amount of current passing through the channel in the ON and OFF states to measure how close the TFT behavior is to an ideal binary switch. Substhreshold swing, *SS*, is a useful metric for characterizing the efficiency of switching behaviour as well as an indirect indicator of defect density at the semiconductor-dielectric interface. These values can be extracted from a combination of the transfer: I_{DS} versus V_{GS}, output: I_{DS} versus V_{DS}, and high-frequency capacitance-voltage (C-V) curves of a device. For high quality amorphous silicon, electrons have a drift mobility of ~1cm^2 V^{-1}s^{-1} while hole mobility is several orders of magnitude lower at ~0.02cm^2 V^{-1}s^{-1}.[47][48] Typical I_{ON}/I_{OFF} ratios are on the order of 10^6-10^8. Finally, other metrics such as the contact resistance provide valuable insight into the semiconductor-contact material interface and the inherent energy losses present in the TFT.

4.3.1   Threshold voltage

To extract V_T we may plot the relationship between the square root of I_{DS} and V_{GS} in the saturation regime (Eqn. (14) in order to obtain the curve in Figure 26. The x-intercept of the linear fit to this curve is used to determine the threshold voltage. This can be understood by noting that at the x-intercept corresponding to V_T, the current through the device should theoretically be zero according to the previously introduced Eqn 13 for $I_{DS,sat}$. This equation requires the condition of $V_{GS}=V_T$ to be satisfied in order for I_{DS} to be zero, thus the V_G at which the current is zero must correspond to V_T.
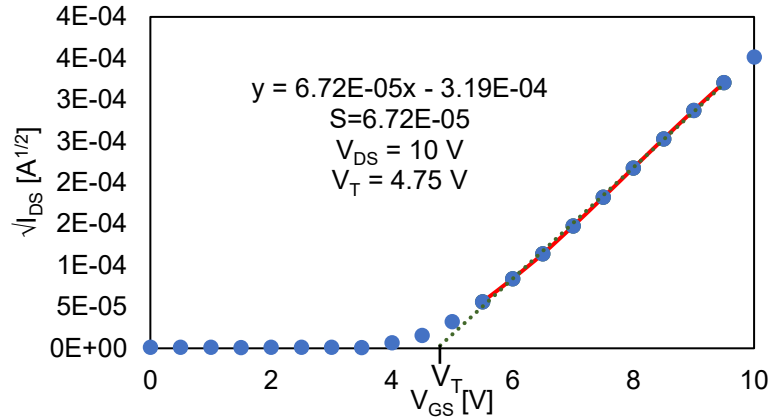
Figure 26 Square root I_{DS} versus V_{GS} plot for a 200um wide by 100um long Al-Cr contact bottom gate TFT, V_{DS} = 10 V

By taking the square root of the equation for drain-source current in the saturation regime, we can also obtain mobility, μ_{FE}, as shown in Eqn (13). However, to do so we must first experimentally determine the specific capacitance per unit area of the dielectric, C_{ox}.

$$\sqrt{I_{DS_{sat}}} = \sqrt{C_{ox}\mu_{FE}\frac{W}{2L}}(V_{GS} - V_t)$$ (14)

4.3.2 Oxide capacitance and mobility extraction

To find the specific capacitance per unit area of a dielectric, a metal-insulator-semiconductor (MIS) capacitor is fabricated as a test structure on the same wafer and a capacitance-voltage sweep carried out to obtain the curve shown in Figure 27. This was carried out for the TFT process used in this work in order to enable characterization of devices.
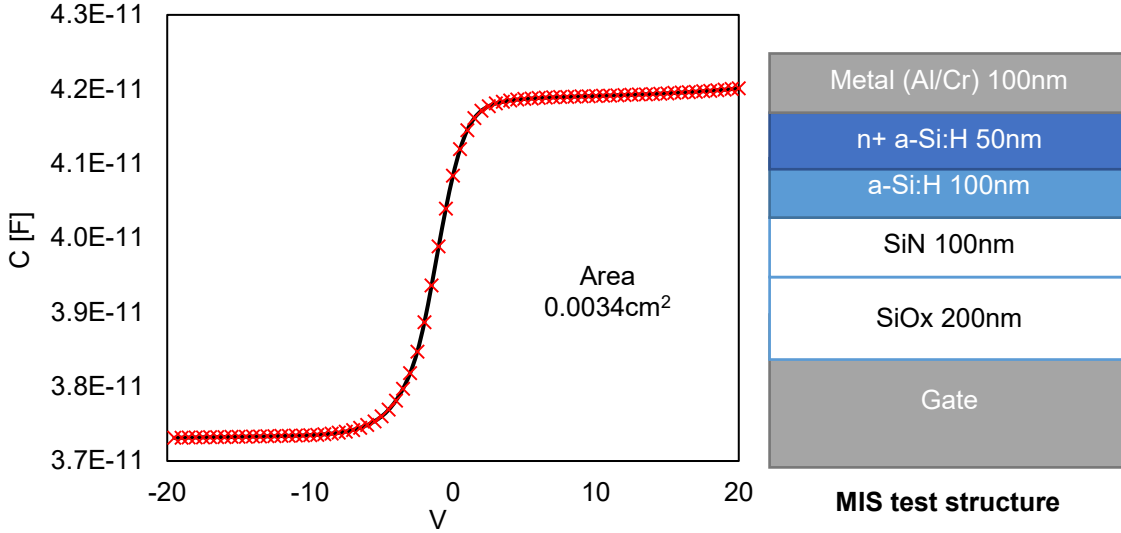
Figure 27 Left: high frequency CV curve of an p+/SiN/SiO₂/a-Si:H capacitor taken with an AC signal frequency of 100MHz, Right: schematic diagram of the MIS stack measured.

Figure 27 shows a typical MIS C-V plot showing how the capacitance of the metal-insulator-semiconductor sandwich changes as carriers are accumulated or depleted inside the semiconductor in response to a changes in applied potential (V_G). For a n-type MIS capacitor, the maximum capacitance, C_{max}, is equivalent to the oxide capacitance in the carrier accumulation regime on the positive end of the graph; whereas the minimum capacitance, C_{min}, is the combined capacitance of semiconductor and oxide in the depletion regime on the negative side of the graph.[49]

Theoretical calculation of the relative permittivity and capacitance per unit area for a dual dielectric of 200nm of SiO₂ and 100nm silicon nitride predict an effective relative permittivity, ε_r, of 4.64, and capacitance of 1.36×10^{-8} F/cm². The test device fabricated had an area of 0.0034 cm² and a C_{max} of 42pF, translating to a dielectric capacitance per area of 1.23×10^{-8} F/cm², in close agreement with theory. Finally, we are able to obtain mobility through the relationship in Eqn. (14) by using the length and width of the semiconductor channel and the obtained threshold voltage and areal capacitance. Using the slope, S, of the linear fit in Figure 26, which we know is equal to $\sqrt{C_{ox}\mu_{FE}\frac{W}{2L}}$, we can solve for the mobility.[50]

4.3.3   Subthreshold swing

Subthreshold swing (SS), defined as the potential difference (in millivolts) at the gate required to raise the current flowing through a transistor by 10-fold (a decade), is used to characterize how well a channel conductivity can be controlled below the saturation threshold. A logarithmic plot of drain current versus gate voltage for low V_D will show a linear behaviour in this operating regime and can be used to obtain the SS metric in units of mV/decade.[50] A device with excellent switching behaviour will have a lower subthreshold swing, implying switching occurs over a shorter range of applied potential. The SS is an indicator of the defect density at the semiconductor-dielectric interface; high SS implies a high defect concentration, with defects subsequently acting to trap charge during operation. The effect lowers the drain current during the I_{DS} vs. V_{GS} scan as carriers are lost to trapping, resulting in slower switching across a wider range of applied V_{GS}. A lower SS is associated with improved I_{ON}/I_{OFF}, lower leakage current, and less energy wasted during switch operations. Subthreshold slope is the reciprocal value of subthreshold swing, expressed in units of decade/mV; in the case of subthreshold slope it is desirable to have a larger value corresponding to higher increase in current per incremental increase in applied voltage.

The plot shows Log$_{10}$ IDS [A] versus V_{GS} [V], with annotations:

$$y = 6E\text{-}17e^{3.7341x}$$

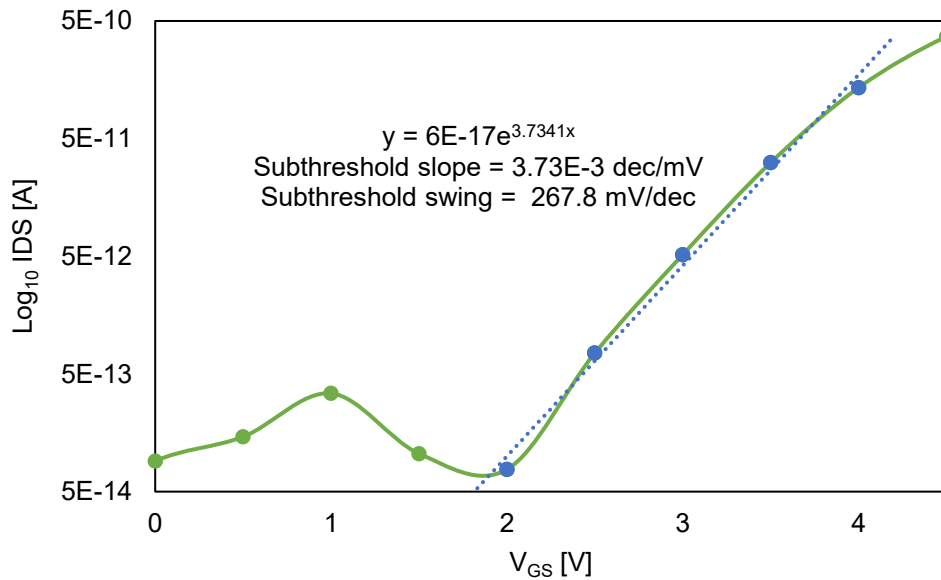Subthreshold slope = 3.73E-3 dec/mV
Subthreshold swing = 267.8 mV/dec

Figure 28 Extraction of subthreshold swing (SS) for an a-Si:H TFT device with W/L=200/100 um at V_{DS}=0.1

Devices with W = 200, L = 100, 50, 25, and 15 fabricated with sputtered Al-Cr contacts were tested to serve as a control for the fabrication process and act as a baseline for comparison of printed-contact devices. I_{ON}/I_{OFF}, V_T, subthreshold swing, and μ_{FE} were extracted as described above and summarized in Table 7.

Table 7 Characteristics of a-Si:H thin film transistors with sputtered Al-Cr contacts

W/L	I_{ON}/I_{OFF}	C_{ox} $F\text{-}cm^{-2}$	V_T V	μ_{FE} $cm^2V^{-1}s^{-1}$	SS $mV\text{-}dec^{-1}$
200/100	10^6	1.23×10^{-8}	4.75	0.367	267
200/50	10^7	1.23×10^{-8}	4.63	0.365	310
200/25	10^7	1.23×10^{-8}	4.11	0.293	299
200/15	10^7	1.23×10^{-8}	4.06	0.226	254

All four out of four devices tested exhibited good switching behaviour, with low leakage current of ~10^{-14}A and good subthreshold swing, and showed field effect mobility and threshold voltage characteristics on the order of magnitude expected for a-Si:H transistors. Mobility was slightly on the low end for bottom gate a-Si:H TFTs at 0.3-0.36 $cm^2V^{-1}s^{-1}$. Having confirmed the processing steps outlined produced consistently working TFTs, the contact resistance of devices with sputtered metal source and drain was investigated in order to establish a baseline for comparison with printed contacts.

4.3.4   **Contact resistance**

The Transmission Line Measurement (TLM) is an important technique in semiconductor physics used to extract the parasitic source and drain series resistances. When current flows through a device's source, channel, and drain, it encounters two heterogeneous junctions – the source-channel and the channel-drain interfaces. The TLM technique is used to probe how effective a particular contact material is for creating a junction to a semiconductor channel material.[51] Practically, the parasitic contact resistances from source-channel and drain-channel interfaces can be seen as a potential drop which impedes the flow of carriers between the source (or drain) and the channel. The TLM method is able to determine the contact resistance and is based on the

assumption that total resistance provided by the device is a combination of the channel resistance as well as the contact resistance:

$$R_T = R_{sc} + 2R_c + 2R_m \approx R_{sc} + 2R_c \qquad (15)$$

where R_{sc} is the channel resistance of the semiconductor, R_c is the resistance of the source or drain contact, and R_m is the resistance of the contact material.[50] For most cases the channel resistance is much greater than the resistance of the contact material, and the assumption can be made that $R_m \approx 0$ to simplify this analysis. TLM analysis requires a TLM test structure consisting of a semiconductor material with contacts spaced out at various lengths; alternatively, devices with multiple channel lengths can be used to obtain the same result. By plotting the relationship of channel resistance normalized to the channel width versus the channel length, it is possible to extrapolate to a theoretical zero channel length that will correspond to the total resistance of the source and drain to semiconductor junctions, $2R_c$. If we express the contact separation between contacts using the ratio of L/W on the x-axis and plot resistance on the y-axis, the slope of the line becomes equal to the sheet resistance, R_s, of the semiconductor, providing a secondary benefit.

As contacts vary in size, it is more useful to compare contact resistivity (ρ_C),

$$\rho_C = R_c A_c \qquad (16)$$

Where A_c is the area of the contact. As most devices do not have contacts in-plane with the semiconductor material, but rather sitting on top of the semiconductor, the edge of the contact closest to the channel will experience higher current flow than the farthest edge, resulting in an effect known as 'current crowding.' The relationship for current drop-off from the edge of the contact is proportional to the exponent of the distance from the edge (x) divided by the transfer length (L_T),

$$I(x) \propto e^{-\frac{x}{L_T}}, L_T = \sqrt{\frac{\rho_c}{R_S}} \tag{17}$$

The transfer length is the average distance that a carrier will travel in the semiconductor under the contact before being collected by the contact and flowing out of the device. Thus the effective geometric area of the contact can be expressed by $A_c = L_T W$. Using the equations above, the total resistance now simplifies to:

$$R_T = \frac{R_S}{W}(L + 2L_T) \tag{18}$$

Using this relationship and a plot of the channel length versus the total resistance, we can extract several figures of merit including the sheet resistance of the semiconductor (R_s), the contact resistance (R_c), the transfer length (L_T), and the contact resistivity (ρ_c) as shown in Figure 29.
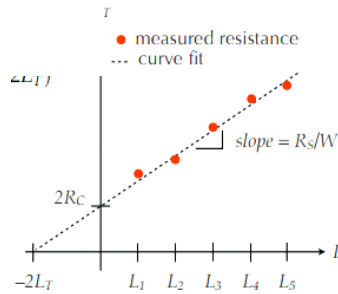
Figure 29 Relationship between the total resistance and length of a device channel showing points corresponding to transfer length and contact resistance.

The TLM method was used to characterize the sputtered metal contact TFTs fabricated as a comparison for printed contacts. Four device sizes were probed with W=200 um and L = 100, 50, 25, and 15um. The total resistance (R_T = 1/slope) was extracted from the linear (low V_{DS}) region of the output I_{DS}-V_{DS} curves for various gate voltages, normalized to the contact width, and plotted versus the channel length to obtain the figure below.

Figure 30 TLM analysis of sputtered metal contact TFTs showing total resistance versus channel length.

The transfer length, contact area, contact resistance and resistivity, and semiconductor sheet resistance were obtained using the previously disc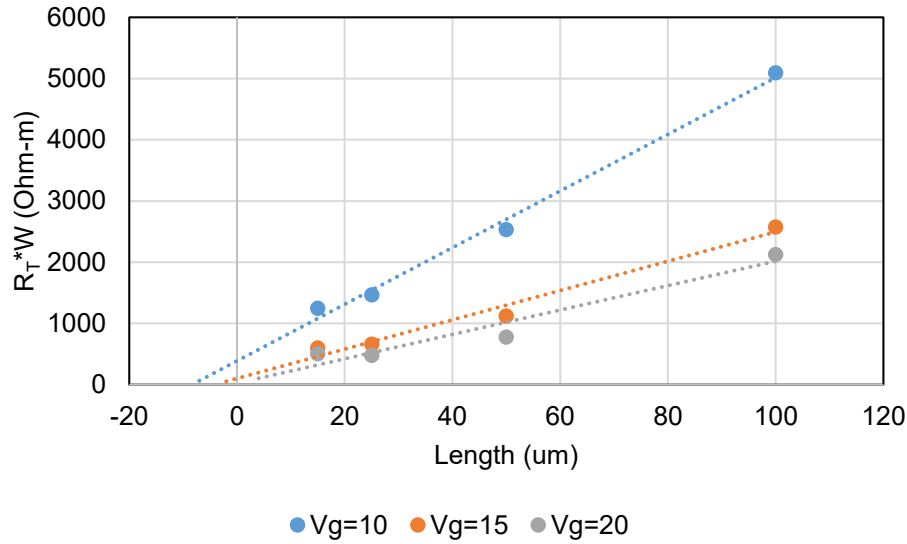ussed relationships. The TLM analysis results for Al-Cr sputtered source and drain TFTs are summarized in the table below.

Table 8 Transmission line method analysis for contact resistance of sputtered metal contact TFTs.

V_G	R_c	R_S	L_T	A_C	ρ_C
	kOhm	Ohm/□	um	10^{-10} m^2	Ohm-m^2
10	965	1155	4.17	8.35	8.08 10^{-4}
15	251	600	2.09	4.18	1.05 10^{-4}
20	55.5	498	0.55	1.11	6.18 10^{-6}

The TLM technique showed that the inherent contact resistivity is low for our a-Si:H TFTs with sputtered metal source and drain contacts, with contact resistivity as low as 10^{-6} Ohm-m^2. It also showed that there is slight dependence of the characteristic length and contact resistance on the applied gate bias. This observation can be understood as being a result of the device design with full overlap between channel and contact, e.g. the channel material runs underneath the source and

drain contacts. As the channel becomes more conductive itself at higher V_G, more of the contact participates in charge collection and subsequently contact resistance will also drop.

TLM analysis is a useful tool to diagnose how well contact materials are working in a device and will later be applied as demonstrated in this section to compare the effectiveness of inkjet-printed contacts made using CNC-PVP-PPY and silver nanoparticles inks.

4.4 TFTs using Silver Nanoparticle and CNC Contacts

4.4.1 Background

The ultimate goal of this work was to go further than simple conductivity measurements by 1) evaluating CNC-PVP-PPY ink, which was shown to have highly stable conductive behaviour and good jettability, as a contact material in proof-of-concept TFTs, and 2) comparing and contrasting the performance of this conductive nanocellulose with a commercially available alternative. The goal of this study was to demonstrate for the first time that conductive CNC ink can be used as an inkjet-printed contact in functional TFT devices.

In order to evaluate the use of printed conductive CNC contacts in TFTs it was necessary to compare the CNC ink with a commercially available, conductive inkjet ink. For this purpose, we chose to evaluate devices with printed silver nanoparticle (Ag-NP) contacts as a baseline in addition to the conventional vacuum processed TFTs. This allowed for the direct comparison of polypyrrole inks to both a vacuum process (sputtered Al/Cr) as well as an emerging inkjet process (Ag-NP).

Spherical silver nanoparticles on the order of 10-100nm are well known for their applications as conductive traces and contacts in printed electronics.[52] The advantages of silver nanoparticles are numerous, including facile synthesis and dispersion in aqueous and organic solvents through the use of capping agents,[53], [54] subsequent stability in solution, low printhead clogging due to their small size, and high conductivity once printed and annealed.[55] Recently much work has been done to find alternatives to this material due to two serious problems. First, silver nanoparticles are relatively expensive to produce due to the silver salts used in their synthesis.

Second, silver nanoparticle contacts require annealing steps that often involve heat treatments, ruling out the use of most flexible and biodegradable substrates which would benefit the most from integration with inkjet printing. For both of these reasons, polypyrrole-coated CNC particles was proposed as an interesting organic alternative with potential for integration into flexible and biodegradable devices.

4.4.2 Printing and annealing silver nanoparticle contacts

TFT devices of an identical design were prepared by the same method as described in Section 4.2 with the additional step of a PAN etch to remove the metal source/drain electrodes and expose the underlying doped n+ a-Si:H layer. A short 5s dip in buffered hydrofluoric acid (BHF) was done in order to remove oxides and impurities present on the newly exposed n+ a-Si:H surface. This step was followed by rinsing with DI water and blow drying with dry nitrogen to prepare samples for the subsequent printing of electrodes over the exposed n+ source and drain regions. Two sets of three differently sized devices were created with all W = 200 um. The process for creating devices with silver nanoparticle contacts is shown in Figure 31.
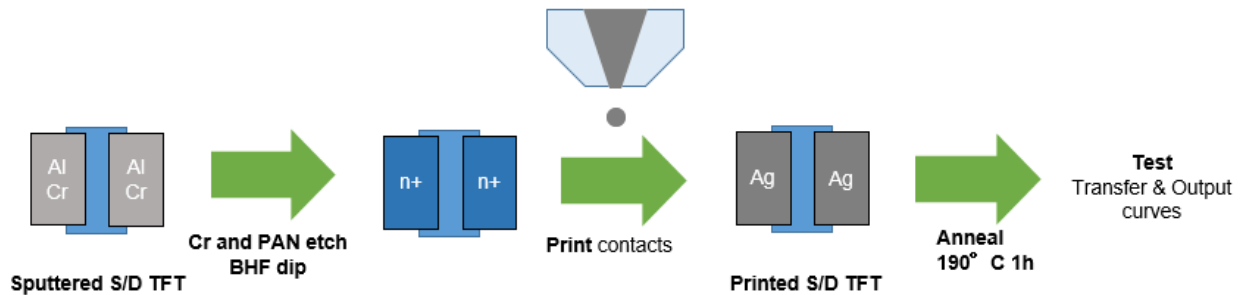

Figure 31 Top view of printed silver TFT contacts process.

Silver nanoparticle ink (DGP 40LT-15C, 500mL) was purchased from Advanced Nano Products (ANP) and filtered with a 5 micron syringe filter before injection into the printer tank. The ANP ink is comprised of 30 (w/w) % silver nanoparticles (diameters of 50nm or less) suspended in triethylene glycol monoethyl ether (TGME) solvent. A Ceradrop L-series materials printer with a Dimatix Sapphire 30pL piezoelectric printhead was used to pattern the ink.

In order to create functioning silver contacts, we carried out a study to determine the effect of annealing temperature on silver nanoparticle sintering. Single drops were printed on CVD-deposited silicon nitride on a silicon wafer and annealed for 1 hour under different temperatures in a vacuum oven under N_2 gas before being observed under SEM and optical microscopy.

Thermal annealing of the printed Ag showed that temperatures below 150°C resulted in almost no observable change in the printed Ag surface morphology after one hour. However, increasing the annealing temperature from 150 to 190 degrees resulted in a change in morphology where the texture of the printed Ag-NP drops transformed from a rough film of diffuse reflectivity and individual particles to a smooth specular surface. This transition is shown in Figure 32.
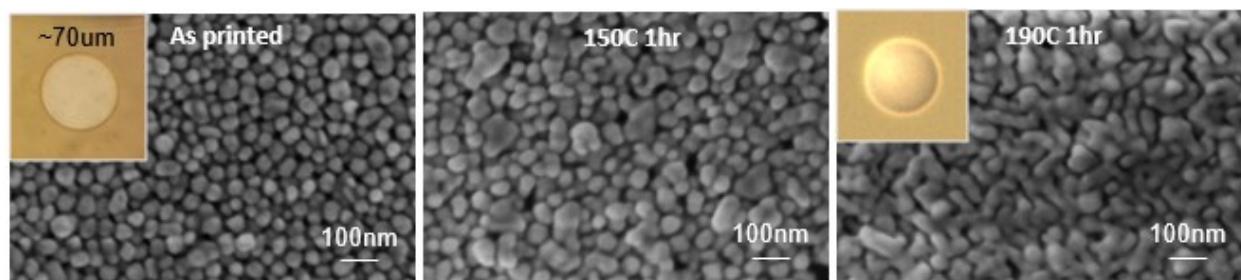

Figure 32 Annealing temperature effect on the morphology of printed silver nanoparticles. Left: SEM image of as-printed droplet (d=70um) showing individual nanoparticles in the silver ink with optical micrograph inset of a drop as-printed, Middle: printed drop annealed at 150 C, Right: printed drop annealed at 190 C with inset of optical micrograph of an annealed drop.

After establishing the required annealing conditions, silver contacts were printed on the TFT source and drain n+ layers using a custom pattern in Ceradrop's CeraSlice software. A CAD image of the printing pattern was simulated within the printer software in order to preview the effect of settings such as infill style (geometry of the droplet pattern, *e.g.* hexagonal, rectangular) and fill sequence (the sequence for patterning the electrode, e.g. sequential, alternating rows or columns) and optimize the printing results. The fill style chosen was rectangular, sequential, and 1 layer thick. The printed contacts were dried at 50°C on a hotplate for 5 min to set the ink before annealing at 190°C for 1 hour under N_2 gas. After annealing the oven was purged with nitrogen gas again and allowed to come to room temperature. Profilometry showed the printed Ag contact thickness

was 50nm on average. Complete TFTs as shown in Figure 33 were kept in a desiccator cabinet under flowing nitrogen to prevent silver corrosion and oxide formation on the a-Si:H.
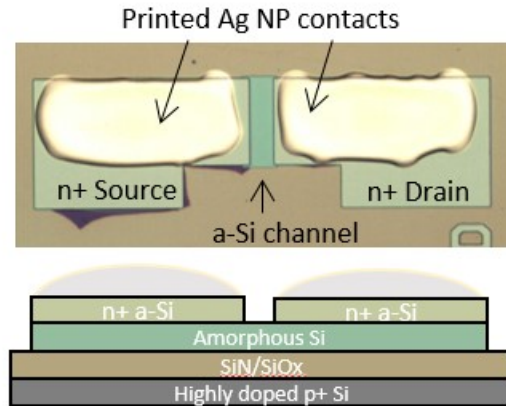

Figure 33 Optical micrograph (top) of a TFT with printed source and drain contacts, W/L of 200/100µm and cross-section schematic (bottom)

4.4.3 Printing polypyrrole-coated CNC contacts

Similar to the process described in Section 4.4.2, a set of three devices with W = 200 um were prepared using established microfabrication techniques before printing CNC-PVP-PPY source and drain contacts. The procedure was used to prepare devices up to the point before printing. It is known that amorphous silicon TFTs can show changes in performance after thermal annealing due to the passivation of dangling bonds and structural relaxation in the TFT layers,[56] therefore an identical annealing step of 1 hour at 190°C was done before printing CNC-PVP-PPY in order to remove this factor and keep the amorphous silicon processing conditions consistent.

CNC-PVP-PPY contacts to the a-Si:H TFTs with W = 200 um, and L= 15, 25, and 100 um were fabricated as follows. The ink formulation for CNC-PVP-PPY described in Section 3.3 was prepared by mixing components to create a black, semi-opaque ink shown in Figure 34, containing 0.5 (w/w) % of CNC-PVP-PPY in a mixture of ethanol, water, and ethylene glycol. The ink was sonicated for 5 minutes and filtered with a 5um nylon syringe filter to remove any aggregates that could potentially cause clogging of the printhead. Printing of the source and drain contacts was carried out using the Ceradrop L-series materials printer outfitted with a Microfab single-nozzle

ejector with a 60-micron nozzle size (MJ-ATP-01-060). A single nozzle dispenser was chosen for prototype ink processing as the amount of raw material available for CNC ink formulation was on the order of milliliters, whereas the 256-nozzle printhead would require 50mL for operation. Droplets of approximately 50-55 pL were reliably jetted and resulted in ~100um diameter drops on silicon nitride and a-Si:H, as shown in Figure 34.
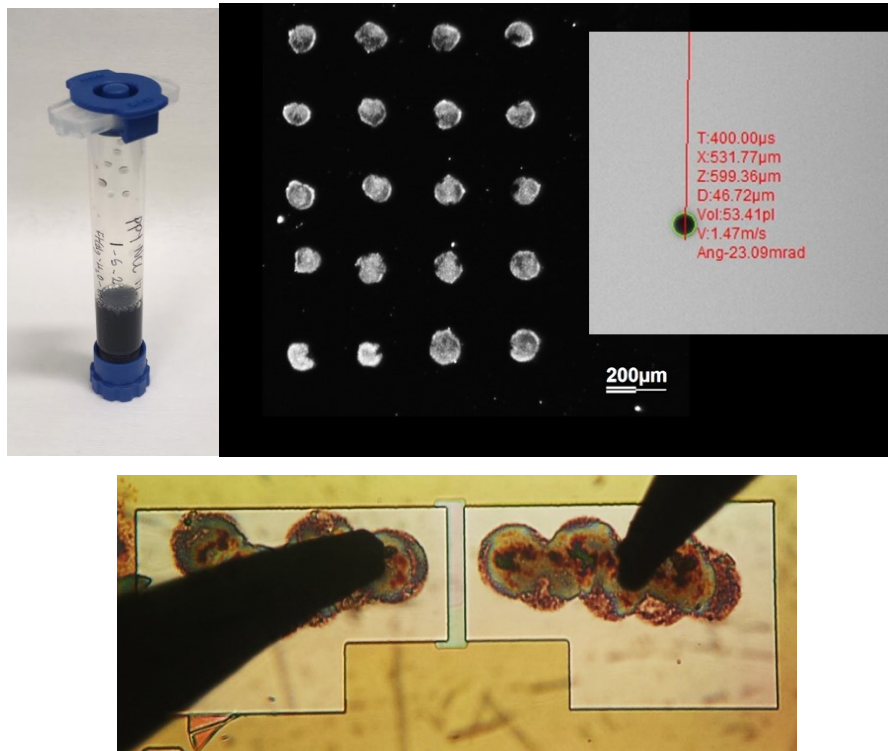

Figure 34 Images of ejected droplets of CNC-PVP-PPy ink (left) captured using a top-view camera on the substrate and in flight (right), and used to pattern contacts for a-Si:H TFTs (bottom).

Drops were printed in a 3-drop line pattern to create a conductive source and drain contact for each size of TFT device. The completed devices did not undergo any further processing and were stored in a cabinet under flowing N_2 to prevent oxidation and contamination. An example of a finished device with W/L=200/100 is shown being probed in Figure 34.

4.4.4   Characteristics of TFTs with AgNP and CNC contacts

All six fabricated devices with printed contacts were measured under a blackout curtain identical to the process outlined for TFTs with sputtered source and drain contacts and described in Section 4.3. In order to contact the three device terminals, we probed the exposed common gate via the highly doped p+ wafer and the source and drain by probing on the printed contacts. The printed contacts were found to provide improved charge injection and collection compared to structures with only the n+ a:Si-H source/drain contacts. (Figure 35) The observed 2-fold increase in I_{DS} between these two cases demonstrates that CNC-PVP-PPY forms an electrical contact onto the doped a-Si:H layer as a charge collecting source and drain contact material.
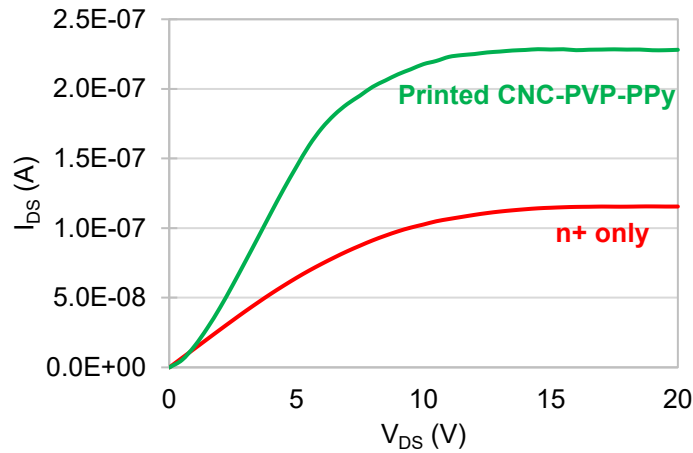

Figure 35 Output curves taken at V_G = 15 V for a TFT device with probing done on n+ layer and compared with printed contact layer.

Measurements were carried out using a three terminal probe station with a Keithley 6430 and 2400 controlled through custom LabVIEW software and used to apply gate, drain, and source bias while measuring current. The obtained transfer curves for the six printed contact devices are compared side-by-side in Figure 36. All six fabricated devices showed typical TFT switching function, however the shortest channel length device with L=15um showed irregular drain current at higher V_{DS}. It is possible this is a processing issue related to the short channel length as the five other devices did not show this behaviour and operated as normal. The complete set of output and transfer curves can be seen in Appendix A.
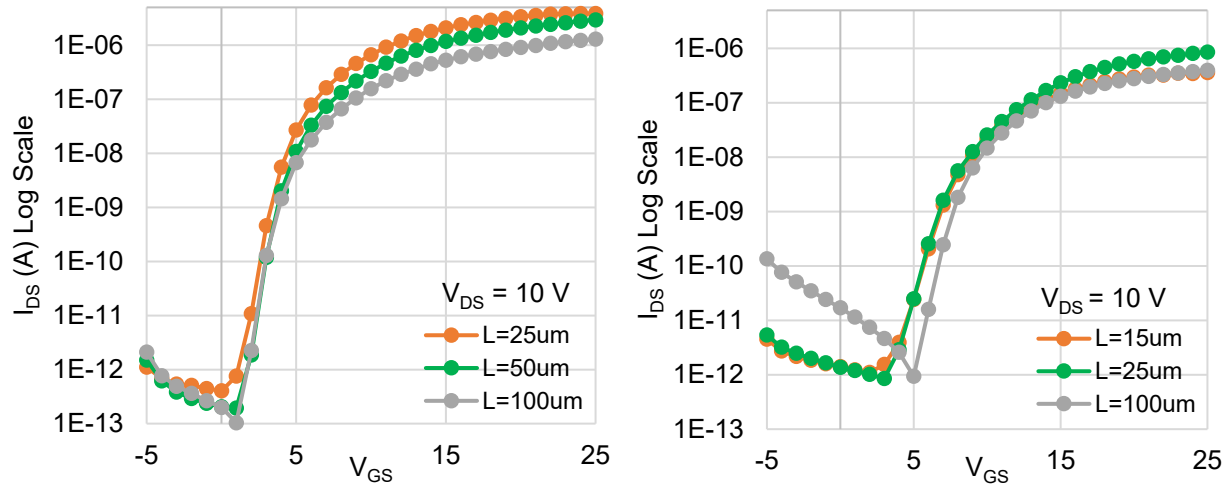
Figure 36 Transfer curves for a-Si:H TFTs with silver nanoparticle contacts (left), and crystalline nanocellulose contacts (right).

Analysis of the output and transfer data for mobility, I_{ON}/I_{OFF} ratio, threshold voltage, and subthreshold swing was carried out as described in Section 4.3 using the previously determined C_{ox}. The extracted characteristics of both sets of printed devices are summarized in Table 9 below.

Table 9 Summary of device characteristics for fabricated TFTs with sputtered versus inkjet printed contacts.

Contact material	W/L	I_{ON}/I_{OFF}	C_{ox} F-cm^{-2}	V_T V	μ_{FE} cm^{2}V^{-1}s^{-1}	SS mV-dec^{-1}
Sputtered Al-Cr	200/100	10^6	1.23×10^{-8}	4.75	0.367	267
	200/50	10^7	1.23×10^{-8}	4.63	0.365	310
	200/25	10^7	1.23×10^{-8}	4.11	0.293	299
	200/15	10^7	1.23×10^{-8}	4.06	0.226	254
Ag-NP	200/100	10^{6-7}	1.23×10^{-8}	3.91	0.340	290
	200/50	10^{6-7}	1.23×10^{-8}	4.03	0.360	291
	200/25	10^7	1.23×10^{-8}	3.83	0.349	303
CNC-PVP-PPY	200/100	10^6	1.23×10^{-8}	7.56	0.194	264
	200/25	10^6	1.23×10^{-8}	7.66	0.085	409
	200/15	10^6	1.23×10^{-8}	6.94	0.028	419

From the results tabulated, it is clear that annealed silver nanoparticle contacts function very much like sputtered metal contacts and show little decrease in mobility, threshold voltage change, or reduced on-off ratio. In the case of CNC-PVP-PPY, there was an apparent decrease in the mobility, an increase in threshold voltage, and poorer subthreshold swing. It follows that poorer contact resistance plays a large role in this effect. As we do not measure the true I_{DS} due to the presence of contact resistance, and the extracted values directly stem from $I_{DS,}$ subsequently the mobility, threshold voltage, and SS are effectively lowered by higher parasitic resistance.

TLM analysis was carried out for Ag-NP and CNC-PVP-PPY contact devices in order to compare the parasitic contact resistances directly. The total resistance, $R_T,$ was obtained from the linear region of I_{DS}-V_{DS} output curves at $V_G = 10$ and 15 V. The slope was used to find the semiconductor sheet resistance, Rs, while the x-intercept corresponded to double the transfer length, $2L_T,$ and the y-intercept to the total contact resistance for both source and drain, $2R_C$. The resultant plots are shown in Figure 37.
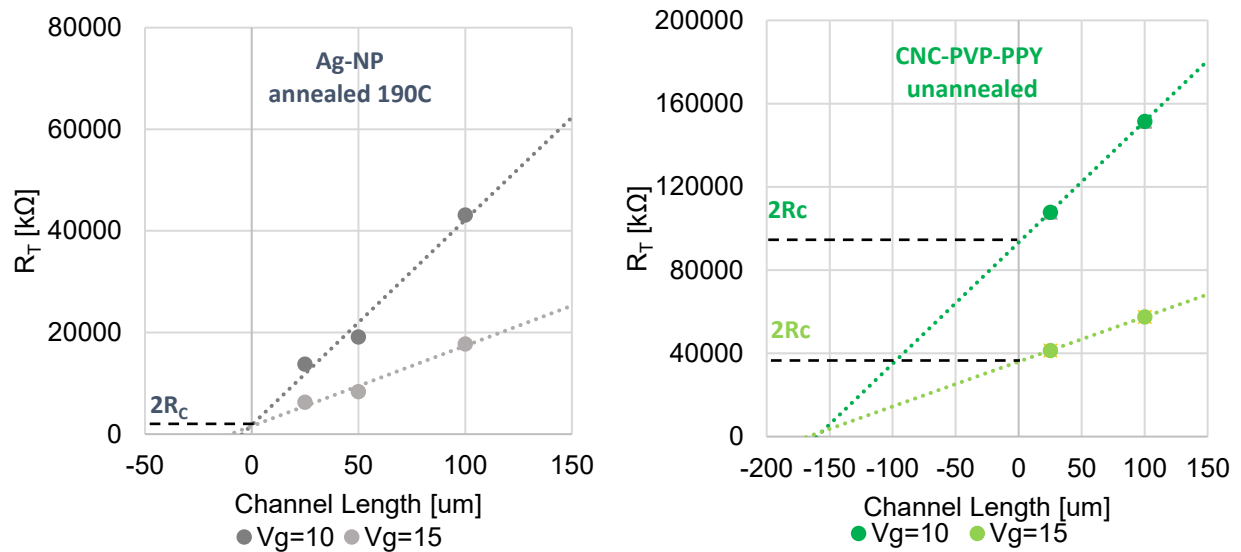

Figure 37 Total resistance versus channel length for printed Ag-NP (left) and printed CNC-PVP-PPY (right) TFT devices.

The contact resistance, transfer length, effective contact area, contact resistivity, and semiconductor sheet resistance were obtained as described in Section 4.3.4 and summarized in Table 10 below.

Table 10 Summary of TLM analysis for TFTs with printed contacts.

Contact material	V_G	R_c	R_S	L_T	A_C	ρ_C
		kOhm	Ohm/□	um	m^2	Ohm-m^2
Ag-NP	10	$8.9 \cdot 10^2$	2020	2.2	$4.41 \cdot 10^{-10}$	$3.9 \cdot 10^{-4}$
	15	$7.8 \cdot 10^2$	790	5.0	$9.93 \cdot 10^{-10}$	$7.8 \cdot 10^{-4}$
CNC-PVP-PPY	10	$4.6 \cdot 10^4$	2910	80.1	$1.60 \cdot 10^{-8}$	$7.5 \cdot 10^{-1}$
	15	$1.8 \cdot 10^4$	1075	83.7	$1.67 \cdot 10^{-8}$	$3.0 \cdot 10^{-1}$

For silver nanoparticle contacts the average transfer length, L_T, was found to be much shorter than that of CNC-PVP-PPY devices. This result is likely due to two factors impeding the efficient collection of charge; 1) contact resistivity for CNC-PVP-PPY ($\sim 10^{-1}$) was found to be 3 orders of magnitude higher than sputtered contacts ($\sim 10^{-4}$) whereas silver nanoparticle contacts were on the same order of magnitude - an expected result considering that conductivity of this newly developed material is currently on the low end for polypyrrole - and, 2) poor coverage of the printed contact upon the n+ layer likely resulted in a smaller contact area between CNC-PVP-PPY and the n+ a-Si:H. The printing process used for CNC materials was done using a single ejector at a high substrate offset from the printhead which resulted in more x-y offset error than in the case of the Dimatix printhead. As such, contacts were printed ~100um away from the channel area to prevent shorting due to misplacement or movement of drops. This may explain the transfer length as the printed contacts did not overlap the semiconductor channel and were placed approximately 80 um away from the channel region on both sides. There was also a high inherent roughness to the CNC network observed through SEM and AFM which may have resulted in even less contact with the n+ layer thus requiring carriers to travel further through the semiconductor before they can be collected by the contact. The reasons discussed here help explain the observation of lower mobility

and poorer SS and V_T for the CNC-contact devices as a direct result of the lower effective contact between CNC and n+ layers due to surface roughness as well as the smaller area coverage.

A minor dependence of width-normalized contact resistance on gate voltage was observed for both CNC-PVP-PPY and Ag-NP contacts similar to sputtered contact devices. This effect can be explained by the following: when $R_{contact} \ll R_{channel}$, charge injection generally occurs at a narrow strip on the edge of the source-drain contacts as we would expect in the contact resistance model. Conversely, when $R_{contact} \gg R_{channel}$ at high V_G, the whole geometric area is now participating in charge injection. It follows that at a higher gate voltage, more of the contact area can be involved in injection, as the accumulation layer at the interface between semiconductor and source-drain becomes more and more conducting.[57] In the case of CNC-PVP-PPY, where the printed contact area did not completely cover the width of the n+ source and drain due to concerns of droplet wetting across the channel, these effects are likely maximized, while in the case of the Ag-NP contacts which mostly covered the widths of the n+ areas due to lower spread, there is less of an effect. It is likely that improved and more consistent coverage of the n+ with CNC-PVP-PPY will further reduce the contact resistivity and high transfer length seen. Through this work it was also seen that wetting of the ink and drop placement plays a significant role in print quality through the limit of achievable printing resolution and accuracy.

4.5 Summary

Though the effective performance of TFTs made with printed polypyrrole-CNC contacts was lower than that of sputtered metal and annealed silver nanoparticle contact devices, the switching behaviour was not compromised and functional TFT behaviour was demonstrated in all devices. The reduction in performance is attributed to poor jetted contact dimensions and high surface roughness of the nanocellulose which led to increased contact resistivity, lower I_{DS} current, and a subsequent decrease in the effective mobility and other performance parameters extracted. Despite these limitations, the proof-of-concept devices may be suitable for a variety of applications; for example, driving low-power electrochromic pixel arrays where mobility is not a concern while good on-off ratio and low leakage currents are more relevant, or passive RF e-sensor tags which require V_T between 1-10V and mobility between 0.01-0.1 $cm^2V^{-1}s^{-1}$ with relatively low operational speeds.[58]

In conclusion, we have shown for the first time 1) formulation of conductive CNC into printable inkjet inks, and 2) functioning TFT devices using novel, inkjet-printed, conductive cellulose nanocrystals as the source and drain contact material. As well, we have compared this innovative material with a commercial silver nanoparticle ink in order to gain a better understanding of the gaps in ink performance and challenges that must be overcome for successful application of cellulose nanocrystal materials.

5   Conclusions and next steps

In this thesis, several successful outcomes and findings were shown with respect to incorporating crystalline nanocellulose into printed electronics. CNC inks showed favourable properties for jetting and were successfully formulated into inks that were jetted consistently using commercially available inkjet dispensers from Microfab Technologies Inc. The formulation developed using water, ethanol and ethylene glycol was shown to possess a good drying profile without the coffee stain effect normally seen in aqueous suspensions of nanoparticles. The challenge in predicting jetting behavior based on fluid properties of CNC suspensions required a trial-and-error method to develop the ink formulation as the viscosity of CNC suspensions could not be measured but is known to be highly shear and concentration dependent. Future ink development efforts could utilize the viscosity-modifying properties of CNC by studying the viscosity change experimentally and applying this method to further fine-tune the fluid's parameters to the printable ranges as defined in work by Jang, Derby, Reis and others. Further improvements to ink formulation were proposed including the possible use of salts and polymeric electrolytes to up ink solids and reduce clogging seen at 1w% and above.

CNC functionalized with conductive materials such as Ag NPs, PEDOT:PSS and polypyrrole showed ohmic conductive behavior, with conductivity measured for polypyrrole-functionalized CNC landing within the range of reported conductivities for the material while the conductivity of CNC-PEDOT materials doped with PSS and PTSA fell towards the low end. The required surface coverage of a percolation network of CNC was calculated to be 44%, 22% lower than for the case of spherical nanoparticles commonly used as printed contact materials. Finally, the formulated polypyrrole-functionalized cellulose nanoparticles were used to create printed contacts to amorphous silicon TFTs and functioning TFT behavior was observed and characterized. The contact resistance was found to be above that of a commercially available silver nanoparticle ink, implying an increase in parasitic losses; lower effective mobility and higher threshold voltage were extracted due to the increased contact resistance, however the devices perform well enough to be integrated for sensing, pixel driving, and other applications. A significant advantage is that CNC-PVP-PPY contacts did not require heat treatment or any form of annealing to attain this performance, making them suitable for use with substrates that are sensitive to processing

conditions. In this work only the water-synthesis based polypyrrole materials were used to attempt to make contacts to TFTs. However, it is foreseeable that Ag-NP functionalized CNC will provide better results as contact materials owing to the fact that they exhibited the highest conductivity out of all the CNC materials, and showed further improvement with annealing at 150 °C. Further investigation of CNC-Ag-NP is recommended using the ink formulation developed through this work, as this approach may lead to devices more closely comparable to that of commercial Ag-NP inks. It was also suggested that scale-up friendly post-processing techniques such as mechanical pressing or rolling -which have shown promise for other percolation network materials- are investigated with the aim of reducing the surface roughness and improving contact between the jetted CNC nanoparticles and the a:Si:H. Rolling may allow us to access the maximum performance of the CNC materials with a treatment that is easily integrated into a roll-to-roll manufacturing line.

The results described show significant promise for the development of bio-mass-based TFTs in the future. High performance inkjet-printed semiconductors such as poly-Si with impressive mobility of $6.5 cm^2V^{-1}s^{-1}$ have already been reported[59] and could be integrated with the cellulose nanoink developed herein as it has been shown to form good contacts to silicon. Dielectrics are among the easier materials to solution-process, with polymeric dielectrics such as polyvinyl alcohol (PVA) and polymethyl methacrylate (PMMA) lending themselves well to roll-to-roll coating methods. It is foreseeable that development of all-inkjet-printed TFTs using CNC materials is a logical next step.

As part of the advancement towards robust all-printed TFTs, new materials such as the conductive cellulose described here-in will be required that can be bio-sourced, solution-processed (with minimal post-processing required), and applied to a variety of substrates. These new materials will have to be mechanically flexible for integration into flexible substrates and roll-to-roll production systems, and ideally approached with an internet-of-things conscious mentality. As more and more everyday items are designed to become 'smart' with simple electronics such as environmental sensors, memories, displays and RF tags, it is of utmost importance that we consider the impact of these mass-produced items once they are used and discarded.
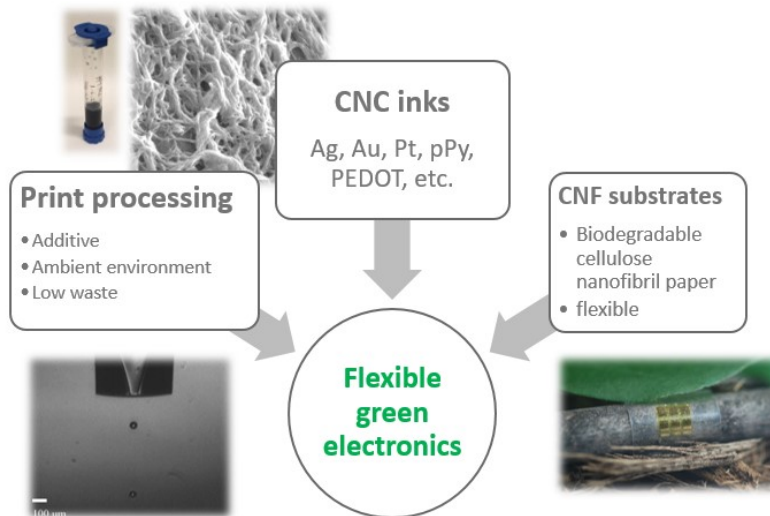
Figure 38 The potential for integration of inkjet printing with functionalized CNC and cellulosic substrates to create flexible green electronics.

Biodegradable and recyclable electronic materials will arguable become a necessity for the well-being of future generations in order to control and reduce the amount of toxic material waste entering our waste-stream, and subsequently, our environment. The research described here-in is a small step towards what the author hopes may foreseeably become an electronic materials platform based on cellulosic materials and comprised of print processing, aqueous inks, and biodegradable substrates to enable the proliferation of truly 'green', environmentally friendly and sustainable electronics.

References

[1] J. P. Rolland and D. A. Mourey, "Paper as a novel material platform for devices," *MRS Bull.*, vol. 38, no. 4, pp. 299–305, 2013.

[2] A. T. Zocco, H. You, J. a Hagen, and A. J. Steckl, "Pentacene organic thin-film transistors on flexible paper and glass substrates.," *Nanotechnology*, vol. 25, no. 9, p. 094005, Mar. 2014.

[3] A. M. Gaikwad, D. a. Steingart, T. Nga Ng, D. E. Schwartz, and G. L. Whiting, "A flexible high potential printed battery for powering printed electronics," *Appl. Phys. Lett.*, vol. 102, no. 23, p. 233302, 2013.

[4] J. Kim and S. Yun, "Discovery of Cellulose as a Smart Material," *Macromolecules*, vol. 39, pp. 4202–4206, 2006.

[5] B. L. Peng, N. Dhar, H. L. Liu, and K. C. Tam, "Chemistry and applications of nanocrystalline cellulose and its derivatives: A nanotechnology perspective," *Can. J. Chem. Eng.*, vol. 89, no. 5, pp. 1191–1206, Oct. 2011.

[6] K. Missoum, M. N. Belgacem, and J. Bras, "Nanofibrillated Cellulose Surface Modification: A Review," *Materials (Basel).*, vol. 6, pp. 1745–1766, 2013.

[7] Q. Chen, P. Liu, F. Nan, L. Zhou, and J. Zhang, "Tuning the iridescence of chiral nematic cellulose nanocrystal films with a vacuum-assisted self-assembly technique," *Biomacromolecules*, vol. 15, no. 11, pp. 4343–4350, 2014.

[8] M. Nogi and H. Yano, "Transparent Nanocomposites Based on Cellulose Produced by Bacteria Offer Potential Innovation in the Electronics Device Industry," *Adv. Mater.*, vol. 20, no. 10, pp. 1849–1852, May 2008.

[9] M. Hamedi, E. Karabulut, A. Marais, A. Herland, and G. Nystr??m, "Nanocellulose

aerogels functionalized by rapid layer-by-layer assembly for high charge storage and beyond," *Angew. Chemie - Int. Ed.*, vol. 52, no. 46, pp. 12038–12042, 2013.

[10] X. Wu, V. L. Chabot, B. K. Kim, A. Yu, R. M. Berry, and K. C. Tam, "Cost-effective and scalable chemical synthesis of conductive cellulose nanocrystals for high-performance supercapacitors," *Electrochim. Acta*, vol. 138, pp. 139–147, 2014.

[11] A. Khan, R. A. Khan, S. Salmieri, C. Le Tien, B. Riedl, J. Bouchard, G. Chauve, V. Tan, M. R. Kamal, and M. Lacroix, "Mechanical and barrier properties of nanocrystalline cellulose reinforced chitosan based nanocomposite films," *Carbohydr. Polym.*, vol. 90, no. 4, pp. 1601–1608, 2012.

[12] D. Gaspar, S. N. Fernandes, a G. de Oliveira, J. G. Fernandes, P. Grey, R. V Pontes, L. Pereira, R. Martins, M. H. Godinho, and E. Fortunato, "Nanocrystalline cellulose applied simultaneously as the gate dielectric and the substrate in flexible field effect transistors.," *Nanotechnology*, vol. 25, no. 9, p. 094008, Mar. 2014.

[13] Y. Habibi, T. Heim, and R. Douillard, "AC Electric Field-Assisted Assembly and Alignment of Cellulose Nanocrystals," *J. Polym. Sci. Part B Polym. Phys.*, vol. 46, pp. 1430–1436, 2008.

[14] Z. Shi, J. Tang, L. Chen, C. Yan, S. Tanvir, W. A. Anderson, M. Berry, and K. C. Tam, "Enhanced colloidal stability and antibacterial performance of silver nanoparticles / cellulose nanocrystal hybrids," *J. Mater. Chem. B Mater. Biol. Med.*, vol. 3, pp. 603–611, 2014.

[15] R. Ansari, "Polypyrrole Conducting Electroactive Polymers: Synthesis and Stability Studies," *E-Journal Chem.*, vol. 3, no. 4, pp. 186–201, 2006.

[16] P. Saville, "Polypyrrole Formation and Use," Dartmouth, 2005.

[17] A. R. Madaria, A. Kumar, F. N. Ishikawa, and C. Zhou, "Uniform, highly conductive, and

patterned transparent films of a percolating silver nanowire network on rigid and flexible substrates using a dry transfer technique," *Nano Research*, vol. 3, no. 8. pp. 564–573, 2010.

[18]   G. Khanarian, J. Joo, X. Q. Liu, P. Eastman, D. Werner, K. O'Connell, and P. Trefonas, "The optical and electrical properties of silver nanowire mesh films," *J. Appl. Phys.*, vol. 114, no. 2, 2013.

[19]   H. S. Lee, Y. W. Kim, J. E. Kim, S. W. Yoon, T. Y. Kim, J. S. Noh, and K. S. Suh, "Synthesis of dimension-controlled silver nanowires for highly conductive and transparent nanowire films," *Acta Mater.*, vol. 83, pp. 84–90, 2015.

[20]   L. Hu, D. S. Hecht, and G. Gru, "Percolation in Transparent and Conducting Carbon Nanotube Networks," pp. 0–4, 2004.

[21]   W. Xia and M. F. Thorpe, "Percolation properties of random ellipses," *Phys. Rev. A*, vol. 38, no. 5, pp. 2650–2656, 1988.

[22]   E. Lam, K. B. Male, J. H. Chong, A. C. W. Leung, and J. H. T. Luong, "Applications of functionalized and nanoparticle-modified nanocrystalline cellulose," *Trends Biotechnol.*, vol. 30, no. 5, pp. 283–290, May 2012.

[23]   P. S. Abthagir and R. Saraswathi, "Junction Properties of Metal/Polypyrrole Schottky Barriers," *J. Appl. Polym. Sci.*, vol. 81, pp. 2127–2135, 2001.

[24]   B. J. Worfolk, S. C. Andrews, S. Park, J. Reinspach, N. Liu, M. F. Toney, S. C. B. Mannsfeld, and Z. Bao, "Ultrahigh electrical conductivity in solution-sheared polymeric transparent films," *Proc. Natl. Acad. Sci.*, vol. 112, no. 46, pp. 14138–14143, 2015.

[25]   T. Tokuno, M. Nogi, M. Karakawa, J. Jiu, T. T. Nge, Y. Aso, and K. Suganuma, "Fabrication of silver nanowire transparent electrodes at room temperature," *Nano Res.*, vol. 4, no. 12, pp. 1215–1222, 2011.

[26]   H. H. Khaligh and I. A. Goldthorpe, "Hot-rolling nanowire transparent electrodes for surface roughness minimization," *Nanoscale Res. Lett.*, vol. 9, no. 310, 2014.

[27]   K.-S. Moon, H. Dong, R. Maric, S. Pothukuchi, A. Hunt, Y. Li, and C. P. Wong, "Thermal Behavior of Silver Nanoparticles for Low-Temperature Interconnect Applications," *J. Electron. Mater.*, vol. 34, no. 2, pp. 168–175, 2005.

[28]   A. Dufresne, "Effects of hydrolysis conditions on the morphology , crystallinity , and thermal stability of cellulose nanocrystals extracted from kenaf bast fibers . Cellulose," no. June, 2016.

[29]   A. Fallahzadeh, J. Saghaei, and M. H. Yousefi, "Effect of alcohol vapor treatment on electrical and optical properties of poly(3,4-ethylene dioxythiophene):poly(styrene sulfonate) films for indium tin oxide-free organic light-emitting diodes," *Appl. Surf. Sci.*, vol. 320, pp. 895–900, 2014.

[30]   C. S. S. Sangeeth, M. Jaiswal, and R. Menon, "Correlation of morphology and charge transport in poly (3, 4-ethylenedioxythiophene)–polystyrenesulfonic acid (PEDOT – PSS) films," 2009.

[31]   I. M. Hutchings and G. D. Martin, *Inkjet Technology for Digital Fabrication*. Wiley, 2012.

[32]   P. Calvert, "Inkjet Printing for Materials and Devices," *Chem. Mater.*, vol. 13, no. 10, pp. 3299–3305, Oct. 2001.

[33]   E. R. Lee, *Microdrop Generation*. CRC Press, 2003.

[34]   Z. Yin, Y. Huang, N. Bu, X. Wang, and Y. Xiong, "Inkjet printing for flexible electronics: Materials, processes and equipments," *Chinese Sci. Bull.*, vol. 55, no. 30, pp. 3383–3407, Nov. 2010.

[35]   G. H. Mckinley and M. Renardy, "Wolfgang von Ohnesorge," *Phys. Fluids*, vol. 23, no. 12,

p. 127101, 2011.

[36] D. Jang, D. Kim, J. Moon, D. Jang, D. Kim, and J. Moon, "Influence of Fluid Physical Properties on Ink-Jet Printability Influence of Fluid Physical Properties on Ink-Jet Printability," vol. 25, no. February, pp. 2629–2635, 2009.

[37] A. Asai, M. Shioya, S. Hirasawa, and T. Okazaki, "Impact of an ink drop on paper," *J. Imaging Sci. Technol.*, vol. 37, pp. 205–207, 1993.

[38] G. Vazquez, E. Alvarez, and J. M. Navaza, "Surface Tension of Alcohol + Water from 20 to 50 C," *J. Chem. Eng. Data*, vol. 40, pp. 611–614, 1995.

[39] D. Bohne, S. Fischer, and E. Obermeier, "Thermal Conductivity, Density, Viscosity, and Prandtl-Numbers of Ethylene Glycol-Water Mixtures," *Phys. Chem. Chem. Phys.*, 1984.

[40] A. Bloomfield and R. K. Dewan, "Viscosity of Liquid Mixtures," vol. 136, no. 20, 1966.

[41] E. D. Cranston, M. Hasani, E. D. Cranston, and D. G. Gray, "Cationic Surface Functionalisation of Cellulose Nanocrystals," *Soft Matter*, vol. 4, pp. 2238–2244, 2008.

[42] S. Magdassi, *The Chemistry of Inkjet Inks*. World Scientific, 2010.

[43] T. Young, "An Essay on the Cohesion of Fluids," *Philos. Trans. R. Soc. London*, vol. 95, pp. 65–87, 1805.

[44] T. H. J. Van Osch, J. Perelaer, A. W. M. De Laat, and U. S. Schubert, "Inkjet printing of narrow conductive tracks on untreated polymeric substrates," *Adv. Mater.*, vol. 20, no. 2, pp. 343–345, 2008.

[45] R. D. Deegan, O. Bakajin, and T. F. Dupont, "Capillary flow as the cause of ring stains from dried liquid drops," pp. 827–829, 1997.

[46] B. J. De Gans and U. S. Schubert, "Inkjet printing of well-defined polymer dots and arrays,"

*Langmuir*, vol. 20, no. 18, pp. 7789–7793, 2004.

[47] C. Janglin, W. Cranton, and M. Fihn, "Hydrogenated Amorphous Silicon Thin Film Transistors (a Si:H TFTs)," in *Handbook of Visual Display Technology*, 2012, pp. 627–646.

[48] Y. Kuo, *Thin Film Transistors: Materals and Processes Volume 1: Amorphous Silicon Thin Film Transistors*. Kluwer Academic Publishers, 2004.

[49] D. A. Neamen, *Semiconductor physics and devices : basic principles*, 3rd ed. McGraw-Hill, 2003.

[50] D. K. Schroder, *Semiconductor Material and Device Characterization*, 3rd ed. Tempe, AZ: John Wiley & Sons, 2006.

[51] C. R. Kagan and P. Andry, *Thin-Film Transistors*. New York: Marcel Dekker, Inc., 2009.

[52] J. R. Greer and R. a. Street, "Mechanical characterization of solution-derived nanoparticle silver ink thin films," *J. Appl. Phys.*, vol. 101, no. 10, p. 103529, 2007.

[53] S. Hemmati, D. P. Barkey, N. Gupta, and R. Banfield, "Synthesis and Characterization of Silver Nanowire Suspensions for Printable Conductive Media," *ECS J. Solid State Sci. Technol.*, vol. 4, no. 4, pp. P3075–P3079, 2015.

[54] W. Shen, X. Zhang, Q. Huang, Q. Xu, and W. Song, "Preparation of solid silver nanoparticles for inkjet printed flexible electronics with high conductivity.," *Nanoscale*, vol. 6, no. 3, pp. 1622–8, 2014.

[55] J. R. Greer and R. a. Street, "Thermal cure effects on electrical performance of nanoparticle silver inks," *Acta Mater.*, vol. 55, no. 18, pp. 6345–6349, Oct. 2007.

[56] S. Roorda, W. C. Sinke, J. M. Poate, D. C. Jacobson, S. Dierker, B. S. Dennis, D. J. Eaglesham, F. Spaepen, and P. Fuoss, "Structural relaxation and defect annihilation in pure

amorphous silicon," *Phys. Rev. B*, vol. 44, no. 8, pp. 3702–3725, 1991.

[57]   T. J. Richards and H. Sirringhaus, "Analysis of the contact resistance in staggered, top-gate organic field-effect transistors," *J. Appl. Phys.*, vol. 102, no. 094510, 2007.

[58]   J. Noh, M. Jung, Y. Jung, C. Yeom, M. Pyo, and G. Cho, "Key Issues With Printed Flexible Thin Film Transistors and Their Application in Disposable RF Sensors," *Proc. IEEE*, vol. 103, no. 4, pp. 554–566, 2015.

[59]   T. Shimoda, Y. Matsuki, M. Furusawa, T. Aoki, I. Yudasaka, H. Tanaka, H. Iwasawa, D. Wang, M. Miyasaka, and Y. Takeuchi, "Solution-processed silicon films and transistors," vol. 440, no. April, pp. 783–786, 2006.

Appendix A – Output and transfer curves of TFT devices
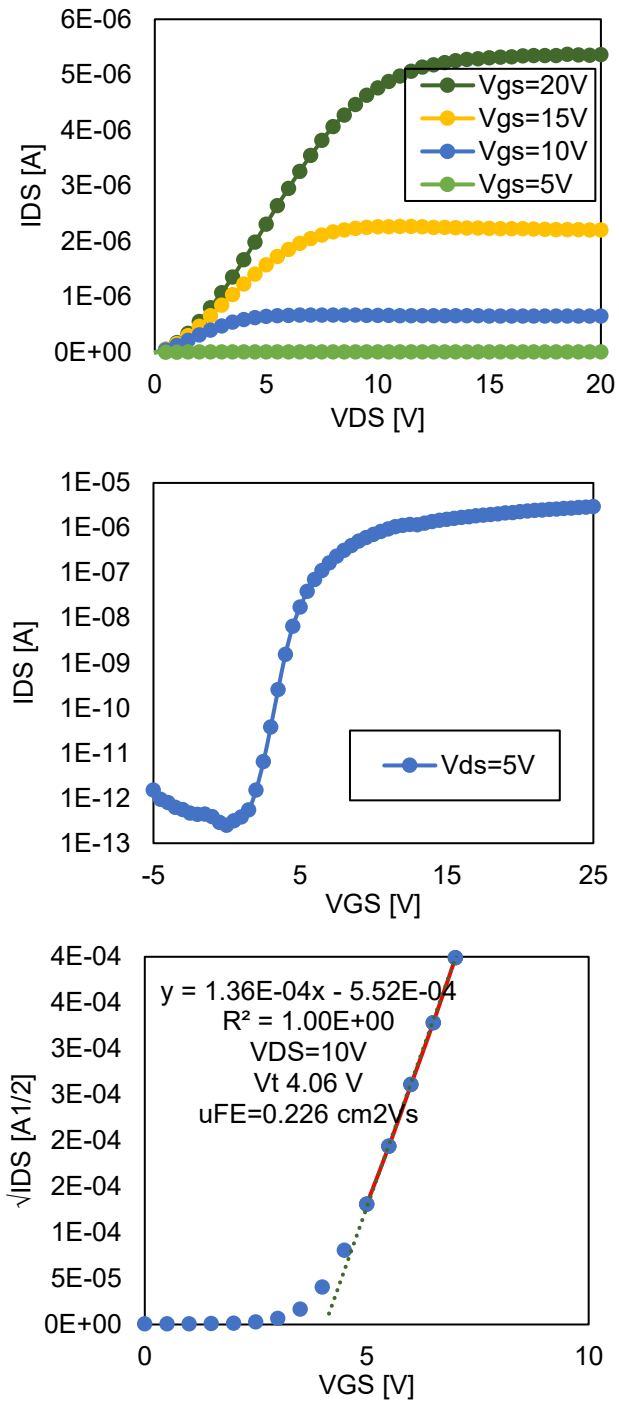
Output and transfer curves for Al-Cr TFT device with W/L=200/15 um.
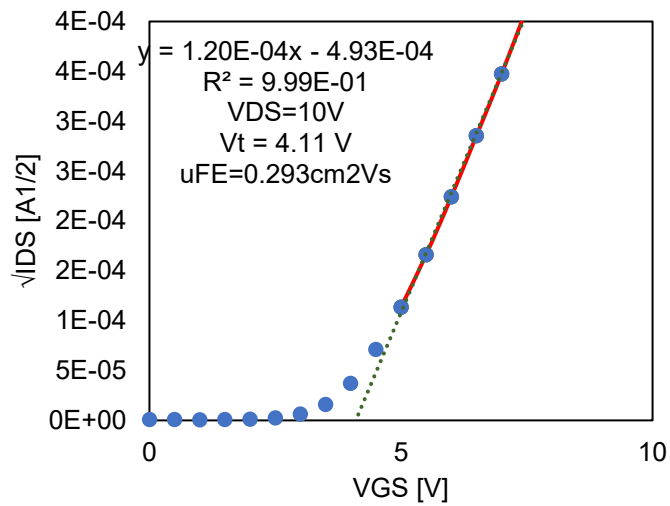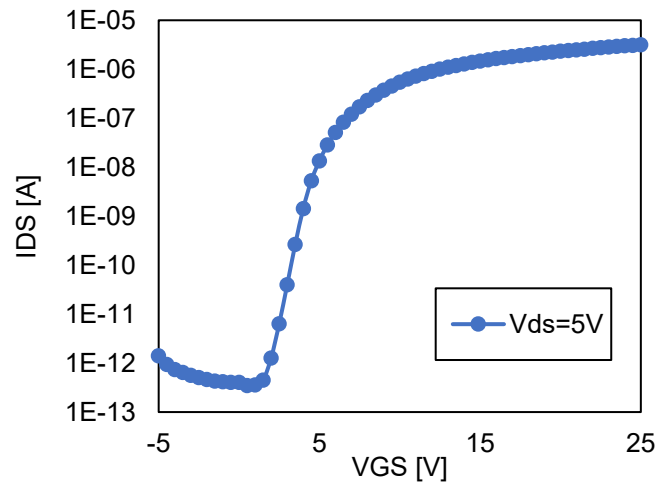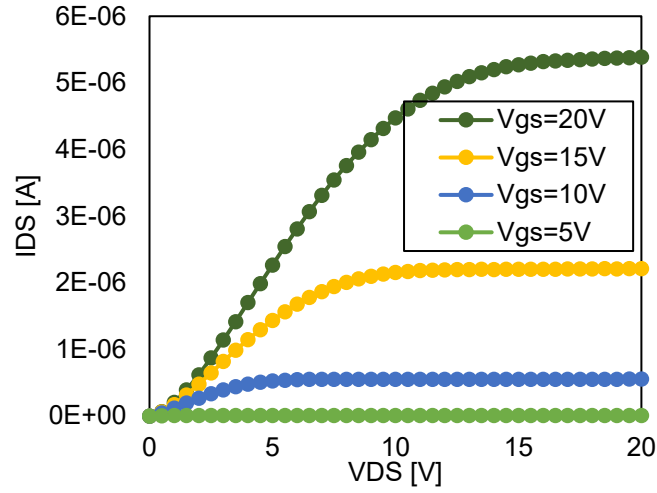
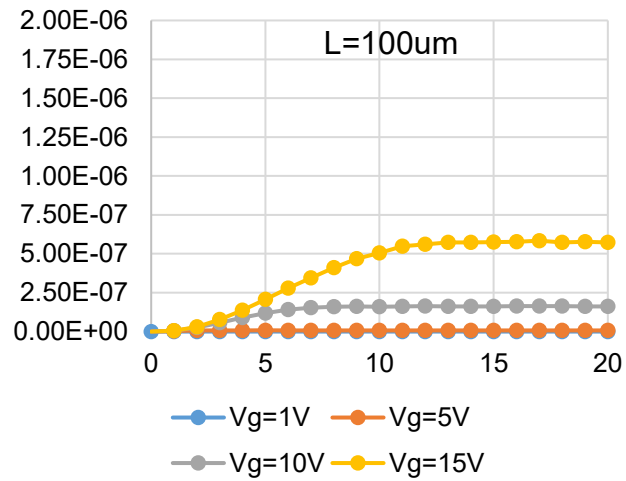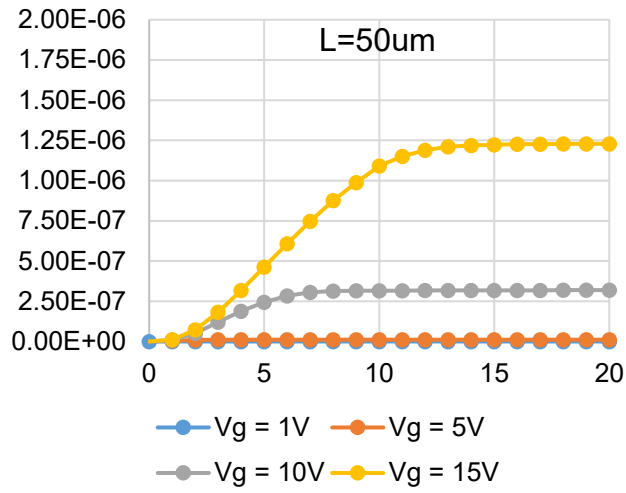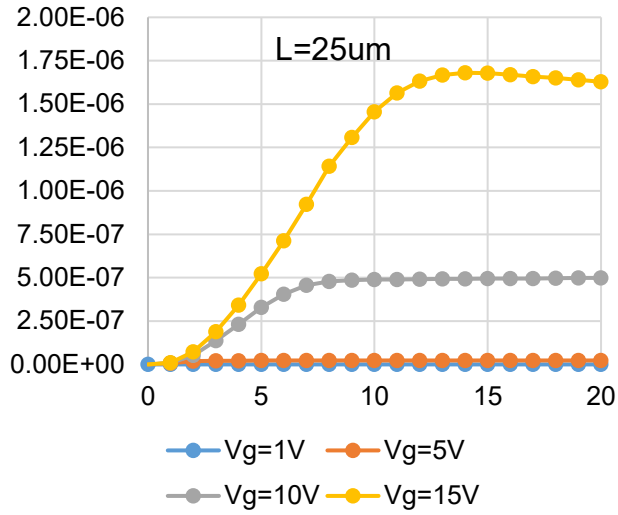**Output and transfer curves for Al-Cr TFT device with W/L=200/25 um.**
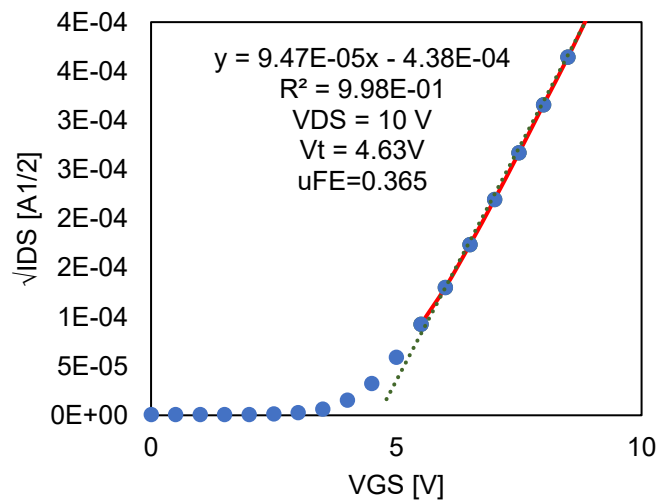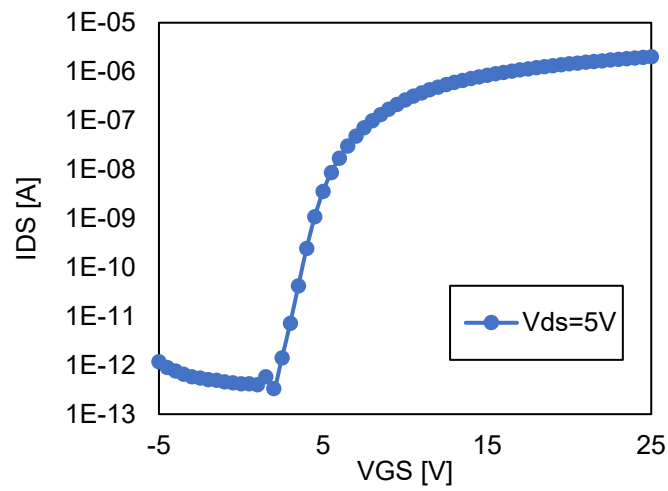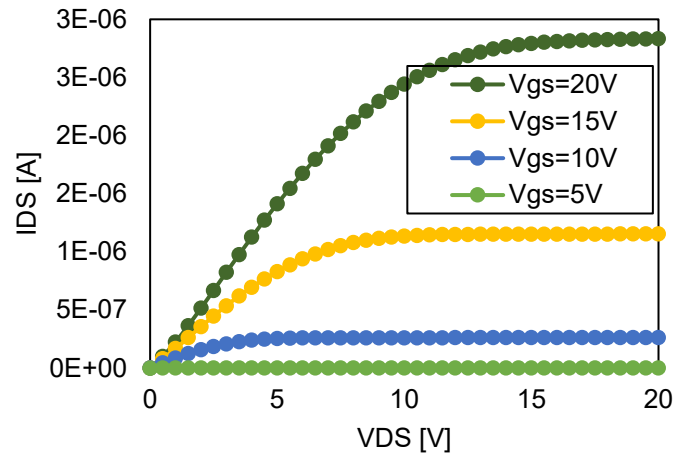
Output and transfer curves for Al-Cr TFT device with W/L=200/50 um.

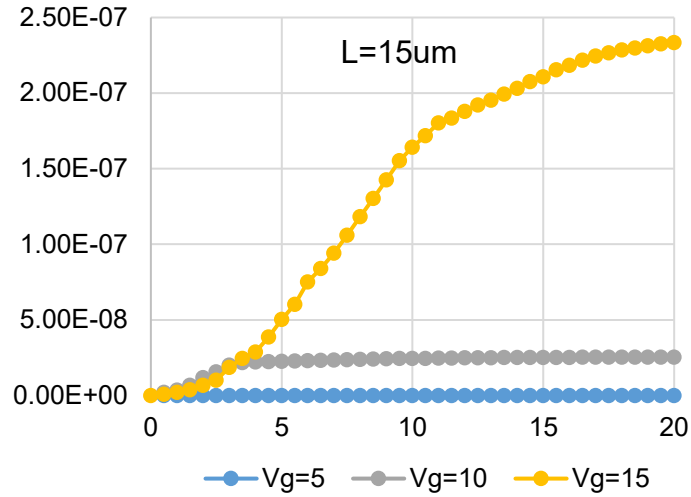Legend for top chart:
- Vgs=20V
- Vgs=15V
- Vgs=10V
- Vgs=5V

Legend for middle chart:
- Vds=5V

Annotation in bottom chart:
y = 6.72E-05x - 3.19E-04
R² = 9.99E-01
VDS = 10 V
Vt = 4.75 V
uFE=0.367cm2Vs
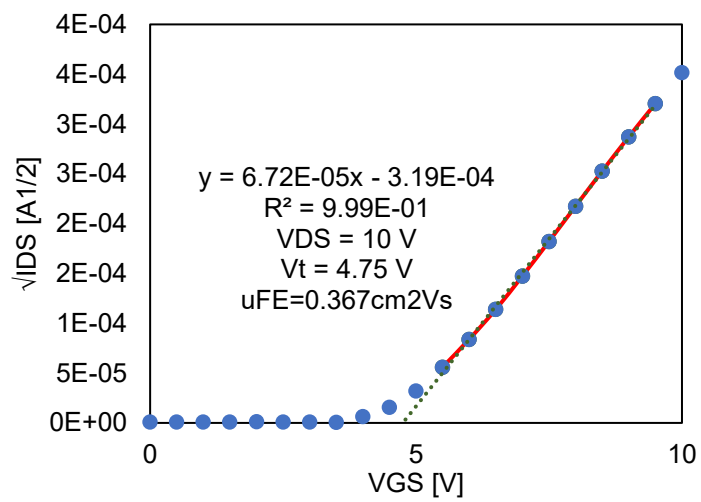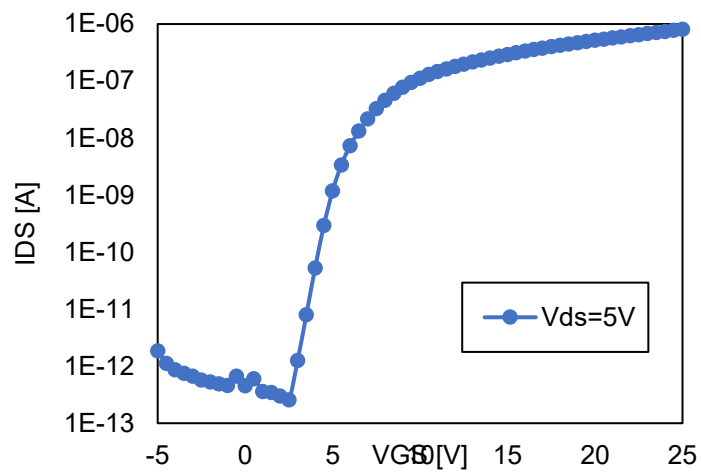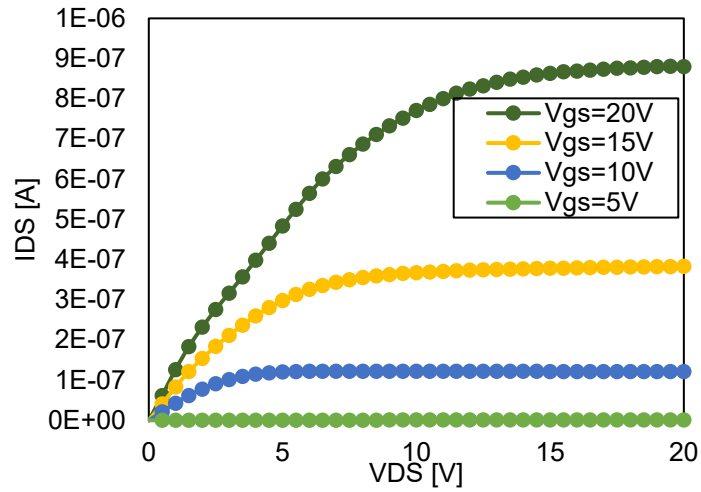
Output and transfer curves for Al-Cr TFT device with W/L=200/100 um.

Output curves for printed silver NP TFT devices of different channel lengths, W= 200um.
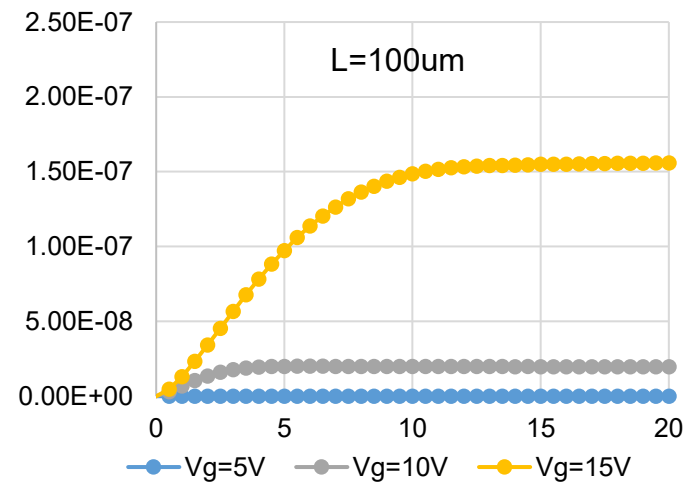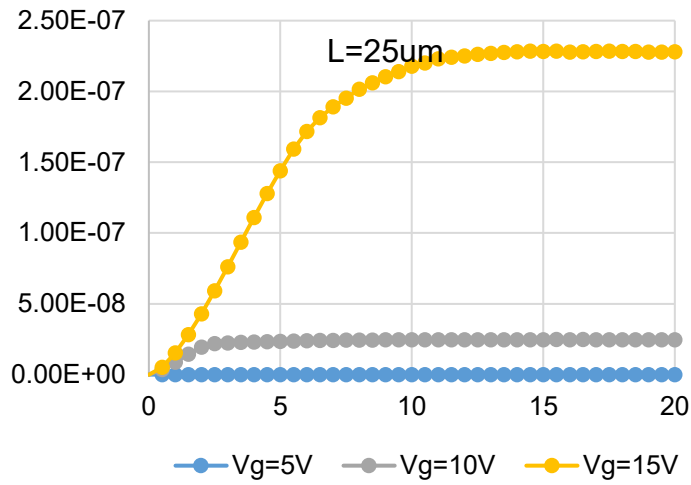
Output curves for printed CNC-PVP-PPY TFT devices of different channel lengths, W= 200um.